Title:
Sandwich cortical lamination and single-cell analysis decodes the developing spatial processing system.

Authors:
Yong Liu[1,9], Tobias Bergmann[1,9], Julie Lee[3], Ulrich Pfisterer[4], Louis-Francois Handfield[5], Yuki Mori[6], Andrea Asenjo-Martinez[4], Irene Lisa-Vargas[4], Stefan E Seemann[2], Jimmy Tsz Hang Lee[5], Nikolaos Patikis[5], Juan Miguel Peralvo Vidal[1], Maria Pihl[1], Birgitte Rahbek Kornum[3,7], Preben Dybdahl Thomsen[1], Poul Hyttel[1], Menno P Witter[8], Konstantin Khodosevich[4], Jan Gorodkin[2], Martin Hemberg[5], Tune H Pers[3] and Vanessa Jane Hall*[1]

Affiliations:
[1]Department of Veterinary and Animal Sciences, Faculty of Health and Medical Sciences; University of Copenhagen, Gronnegaardsvej 7, Frederiksberg C, 1870, Denmark.
[2]Center for non-coding RNA in Technology and Health, University of Copenhagen Groennegaardsvej 3, 1870 Frederiksberg C, Denmark
[3]Novo Nordisk Foundation Center for Basic Metabolic Research, Faculty of Health and Medical Sciences; University of Copenhagen, Copenhagen N, 2200, Denmark.
[4]Biotech Research and Innovation Centre (BRIC), Faculty of Health and Medical Sciences; University of Copenhagen, Copenhagen N, 2200, Denmark
[5]Wellcome Sanger Institute, Wellcome Genome Campus, Hinxton CB10 1SA, United Kingdom.
[6]Center for Translational Neuromedicine, Faculty of Health and Medical Sciences; University of Copenhagen, Copenhagen N, 2200, Denmark
[7] Department of Neuroscience, Faculty of Health and Medical Sciences; University of Copenhagen, Copenhagen N, 2200, Denmark.
[8]Kavli Institute for Systems Neuroscience, Faculty of Medicine and Health Sciences; Norwegian University of Science and Technology, Trondheim, 7030, Norway.

Author List Footnotes:
[9]These authors contributed equally
*Corresponding Author and lead contact: Vanessa Jane Hall

Contact info:
Vanessa Jane Hall: vh@sund.ku.dk

Summary

The entorhinal cortex consists of several important cell types including, the grid cells, speed cells, border cells and head-direction cells and is important for memory, spatial navigation and perception of time. Here, we trace in detail the development of the entorhinal cortex. Using single-cell profiling we provide unique transcriptional signatures for glia, excitatory and inhibitory neurons existing in the region, including RELN+ cells in layer (L) II and superficial pyramidal neurons. We identified a sandwich layered cortex, where LII emerges prior to LIII and superficial cells maintain a deep

layer molecular identity after birth. Our findings contribute to the understanding of the formation of the brain's cognitive memory and spatial processing system and provides insight into the transcriptional identity and spatial position of the entorhinal cells.

Keywords
Entorhinal cortex, development, stellate cell, speed cell, single-cell RNA sequencing, cortical lamination, neurogenesis, gliogenesis, ventral telencephalon

Introduction

Uncovering the temporal events in the emergence of the cell types in the developing entorhinal cortex (EC) is paramount for understanding the formation of cognitive memory and spatial processing. The EC has a pertinent role in these memory and navigational processes, which likely depends on its intrinsic organization as well as extrinsic connectivity. Cortical projections target amongst others, the subiculum and adjacent parahippocampal regions, ventral retrosplenial cortex, medial prefrontal cortex, contralateral cortex and olfactory areas. Subcortically, the EC connects to the septum, the diagonal band of Broca, nucleus accumbens, claustrum, the amygdaloid complex, as well as midline thalamic domains (Witter and Groenewegen, 1986). Specific navigation-related functions have been discovered in the EC including object recognition (Ridley et al., 1988), processing speed movement (Kropff et al., 2015), processing location (Quirk et al., 1992), processing head-direction (Taube et al., 1990), recognizing proximal borders (Solstad et al., 2008) and processing working memory (Olton et al., 1982). These functions signify the importance of the EC in spatial navigation and arise from subsets of firing cells from either the medial EC (MEC) or lateral EC (LEC). Although extensive anatomical and neuronal electrophysiological classification has been performed (Canto and Witter, 2012a, b; Canto et al., 2008), the area lacks detailed molecular characterization. Currently, none, or only very few genes can be used to identify the major cell types within the EC and the locations of these cells types are only partially understood. For example, within the MEC, the grid cells are located in both the dorsal and ventral MEC (Stensola and Moser, 2016) and found across all cortical layers, though showing a preference in layer II (Sargolini et al., 2006). The grid cells are considered to represent principal neurons including both stellate cells and pyramidal neurons (Domnisoru et al., 2013; Rowland et al., 2018; Schmidt-Hieber and Hausser, 2013). Gene markers that distinguish the stellate cells from the pyramidal neurons are REELIN (*RELN*) and CALBINDIN (*CALB1*), respectively (Fuchs et al., 2016; Leitner et al., 2016; Perez-Garcia et al., 2001; Seress et al., 1994; Varga et al., 2010; Witter et al., 2017). Also, RELN is expressed in Fan cells which reside in the superficial layer of the LEC and which are important for object recognition (Germroth et al., 1989; Nilssen et al., 2018). A more specialized grid cell also exists; the conjunctive grid cell which fires when rats cross a grid vertex upon heading in a specific direction. It is absent from LII, mostly present in LIII and LIV, but can also be found in LVI (Sargolini et al., 2006). The head-direction cells are principal neurons found in LII to LVI and are absent from LII (Giocomo et al., 2014; Sargolini et al., 2006). The border cells are also considered

to be principal neurons and are found within all the MEC layers (Solstad et al., 2008) which often overlap with a stellate cell identity (Tang et al., 2014). The speed cells map to GABAergic inhibitory neurons which express parvalbumin (PVALB), but not somatostatin (SST) (Ye et al., 2018). A clearer understanding of the molecular landscape in the EC may help to reconcile the anatomical, functional and connective profiles of the cell types that exist in the EC to allow a better understanding of spatial navigation in the brain.

It is not only the spatial distribution of cell types that remain poorly understood, but also the temporal maturation of the EC cells. Head-direction is the first function to emerge, with head-direction cells firing consistently in the rat already by postnatal day (P)11 (Bjerknes et al., 2015). The recognition of proximal borders develops later, with border cells firing with adult-like properties at P16-18 (Bjerknes et al., 2014). Spatial navigation arises last, with grid cells slowly forming adult-like firing properties after approximately 4 weeks of age (Bjerknes et al., 2014; Langston et al., 2010). Maturation of cell types within cortical layers also shows temporal divergence. For example, in LII, CALB1 positive pyramidal neurons mature earlier than RELN positive stellate cells (Ray and Brecht, 2016). This contrasts with the known birthing time of these cell types in mice, where stellate cells are born two days earlier at E11. Investigating neurogenesis and the emergence of the varying cell types in the developing EC could help to uncover whether the birthing time of cell types in the EC links closely to functional maturity. This was also recently proposed by Donato and colleagues (Donato et al., 2017).

In light of difficulties in obtaining human fetal tissues from the second and third trimester of development, we focused our attention on studying EC development in an alternate large mammal, the pig. The pig develops a gyrencephalic brain similar to humans, and fetal tissue is easily acquired from production farms. Both annotated and unannotated developing and adult pig brain anatomical atlases are readily available from many open sources. A number of published MRI atlases also exist (Conrad et al., 2012; Conrad et al., 2014; Saikali et al., 2010; Winter et al., 2011). These resources demonstrate that porcine and human brain anatomies are highly similar. Like the human brain, there is little proliferation of neurons in the large domestic pig brain after birth (Jelsing et al., 2006). A significant increase in pig brain size following birth is strikingly similar to humans (Conrad et al., 2012). Pig gestational development is relatively long at 114 days which is more comparable to human gestation length (294 days) compared to 20 days in mice. Given the divergence in cortex functions between rodents and humans (Farr et al., 1988) and variations in the connectivity of the sensory cortical networks between mice and humans in the hippocampal region (Bergmann et al., 2016), the pig constitutes a particularly model to study EC development.

Here, we present a the most complete profile to date of the developing EC from an anatomical, molecular and single-cell level. We have uncovered a unique cortical lamination patterning in the EC which differs from the remaining cortex. We identified several unique interneuron and excitatory neuron populations and outlined the molecular phenotypes for all cell types within the MEC, including the

speed cells, stellate cells and pyramidal neuron populations. Our data presents an unparalleled description of novel events during neurogenesis as well as the timing in the emergence and the molecular profile of entorhinal cells to substantially advance the field in the characterization of the developing spatial navigation system.

Results

Subheading 1. Entorhinal cortex development exhibits rapid growth during the second trimester of gestation

Gestational age differences and trimester lengths were first compared between mouse, man and pig to gain a full understanding of the gestational time points and transitions in the pig. We recorded the transition of trimester 1 to 2 as the time point when neural tube formation and gastrulation is completed, which is a recommended feature that has been used in mouse and man (Patten et al., 2014) and key developmental features such as fusion of the palate which corresponds to embryonic day (E)50 in the pig (Sun et al., 2017) and gonadal differentiation, which occurs at E50 in the pig (Pontelo et al., 2018). We therefore deduce the end of the first trimester in the human equals E50 in the pig. The transition from trimester 2 to 3 marks a significant and continual increase in human fetal weight upon completion of organogenesis. A similar and marked increase in fetal weight occurs at E70 in the pig (Kim, 2010). We believe that E70 marks an equal representative of the transition from trimester 2 to 3. A comparative overview of trimester lengths between species, shows that the pig is a better model than the mouse in terms of trimester phases in man (Figure 1A).

The porcine brain has a gyrencephalic cortex and a prominent paleopallium with large olfactory bulbs. The olfactory tract terminates in a large piriform lobe. The EC is located in the piriform lobe, caudal to the olfactory (piriform) cortex and the cortical nucleus of amygdala (COA) and hippocampal transition area (HA) (Figure 1B). We first analyzed the anatomical features of the EC at a late gestational stage and postnatal brain using cresyl violet staining. At E100 (2 weeks prior to birth) we observed a cytoarchitectural mature EC with similar morphology as the postnatal EC (Figure S1). Layer IV was distinctively acellular, which is a typical feature in the adult EC known as the *lamina dissecans*. We identified the parasubiculum (PaS) medial to the EC. The PaS could be identified at E100 from its similar cytoarchitecture to the EC. One exception was that the soma sizes of the LII and LIII cells within the PaS were more equal in size, compared to the EC. In the EC, the LII cells have somas approximately twice as large as the LIII cell somas (Witter et al., 2017). We could identify the perirhinal cortex (PER) located proximally and lateral to the EC through the disappearance of large superficial cells of the LII typical of the EC together with the disappearance of the *lamina dissecans* (Figure 1C). As early as E100, the EC can be divided into a lateral (LEC) and medial (MEC) subdivision. This is based on cytoarchitecture differences described in other species such as rodents, dogs, cats and humans (Gatome et al., 2010; Insausti et al., 1995; Woznicka et al., 2006; Wyss

et al., 1983). The pig MEC, had deeper layers structured with a narrow homogenous and densely packed cellular layer organized with a columnar appearance. In the transition into the LEC, the deep layers widened with a lower cell density and a disordered cell deposition. The *lamina dissecans* in the MEC was distinct and acellular, while in the LEC, the *lamina dissecans* was more diffuse, with more cellular infiltration (Figure 1C and S1). The MEC gradually occupied the entire mediolateral entity along the rostrocaudal axis of the piriform lobe. The MEC caudally borders to the neocortex as the piriform lobe disappears. This boundary was traced by immunolabeling for parvalbumin (PVALB) positive interneurons (Figure S2A), as seen in the rat (Wouterlood et al., 1995). We observed a sulcus forming at the mid-rostrocaudal extent of the EC, persisting to the caudal end of the piriform lobe which was also visible macroscopically (Figure 1B). This sulcus, known as the sagittal sulcus (S.Sag) has been previously reported in the domestic (Holm and Geneser, 1989) and Göttingen minipig (Bjarkam et al., 2017), but not in other gyrencephalic species, such as dogs, cats, and humans (Insausti et al., 1995; Woznicka et al., 2006; Wyss et al., 1983). We observed the S.Sag to coincide with the appearance with the MEC on the rostrocaudal axis (Figure S1), which provided a unique surface landmark for microscopically and macroscopically assessing the MEC and LEC borders.

Interestingly, we observed a high number of oligodendroglia-like cells present in the superficial layers of the LEC and in the adjacent perirhinal cortex (PER), which has not been previously highlighted in other anatomical descriptions of the EC. These cells were proximal and clustered around large entorhinal cells (Figure. 1D). We observed enrichment of these oligodendroglia-like cells in the superficial layers of the LEC and PER from E80 through development. These cells were still apparent in the LEC and PER at P75 (Figure 1D). For earlier stages than E80 similar glia-like cells were observed in all layers and therefore potential oligodendroglia cells could not be distinguished (Figure S2B). Morphologically, these appeared to be pan-neuronal oligodendrocyte precursor cells (OPCs) with clear Nissl free cytoplasm and a large round Nissl stained nucleus (Garcia-Cabezas et al., 2016) (Figure 1E). In the most lateral part of the LEC, these OPC-like cells were evenly distributed within the superficial layer, but converged into distinct islets towards the MEC. The islets disappeared at the border of the LEC-MEC and the clustering of the OPC-like cells was not evident in the MEC. We immunolabeled the EC with the OPC marker, OLIG2 (Figure S2D), and these cells were detected from E60 onwards. Expression of *OLIG2* was also found across all layers (Figure S2E). These oligodendroglial cells were not observed in the neighbouring neocortex regions and have not been reported in other species, indicating that this may be a unique feature of the porcine LEC and adjacent PER (Figure 1D-E).

We subsequently analyzed the timing of the emergence and development of the EC using cresyl violet staining (E50-P75) and structural post mortem MRI (E60-P75) from gestational ages to the postnatal brain. No features of an EC could be determined prior to E50. At E50, we identified prominent and large soma entorhinal-like cells in the superficial layer of the ventral telencephalon before any distinct layer was formed (Figure S2C). The three-layered cortex became six-layered by E60 (Figure S1) and at the same time the *lamina dissecans* was detected (Figure S1). At E60, we

were able to delineate the MEC from the LEC based on the deposition of the deep layer cells and the higher cellularity of the *lamina dissecans* in the LEC. Together, this indicates that the EC cortical layers are formed during the second trimester between E50 and E60 in the pig. At E70 (late in the second trimester), we observed the S.Sag formation microscopically and cells in the superficial LII were prominent, large and darkly stained nuclei with Nissl (Figure S1). From E80, the large cells in LII appeared more prominent (Figure S1) and the S.Sag was macroscopically visible (Figure S1).

The positional anatomy and rate of EC growth was then evaluated using postmortem structural-MRI. Brains from E60 to P75 were scanned on a 9.4T preclinical MRI system (BioSpec 94/30 USR, Bruker BioSpin, Ettlingen, Germany). The EC was annotated from E60 to P75 based on our histological descriptions and macroscopic features (Figure 2A). We calculated the volume of the EC and the remaining cortex based on the MRI annotations and found the EC growth was linear from E60 to P75 (Figure 2B). When we compared the growth rate of the EC to that of the whole cortex of the brain, we found that the EC had a significantly higher growth rate at E70 during the late second trimester (Figure 2B), suggesting a local and specific developmental growth period at this time point. We were unable to detect whether the growth was due to expansion of the white or gray matter, due to the lack of high enough resolution from the MRI images. In summary, we identified prominent OPCs at the early stage of EC development, where the cells were clustered around large entorhinal cells and a significant growth spurt during the late second trimester attributable to either grey and/or white matter expansion.

To further validate the pig as a suitable model for studying the development of EC, we analyzed the number and anatomical endpoints of white matter fibers passing through or emerging from the MEC and LEC using diffusion tensor imaging (DTI) tractography in the postnatal brain (P75). A high number of white matter tracts could be detected emerging from both the MEC (median 6031±1319) and the LEC (median 3329±4099) (Figure 2C-D, Supplementary Table 1). Analyses of the tracts arising from the EC area revealed the septohippocampal system as the main projection site from both the LEC and MEC, however projections also extended to the subiculum, olfactory bulb, the nucleus of the lateral olfactory tract (LOT), amygdala, corpus collosum, putamen (PUT), nucleus accumbens and corpus collosum (Figure 2E-J), Supp video 1, Supp Table 1). Connections between the MEC and LEC could also be observed (Figure 2J, Supp video 1). Regarding connectivity to the hippocampus, the LEC connected to the distal part of CA1 and the MEC mainly connected to the proximal part of CA1, with a minor number of connections to CA2 and CA3 (Supp table 1, Supp. video 1). In addition, the MEC connected to the dentate gyrus (DG) at the septal end of the hippocampus and to the perirhinal cortex (Supp video 1), whilst the LEC mostly connected to the postrhinal cortex (Figure 2E). The observed connectivity to the peri- and post-rhinal cortex concurs with previous studies reported in the rat (Burwell and Amaral, 1998; Insausti et al., 1997). Of interest, was a small number of fibers that emerged from the MEC and disappeared into the corpus collosum (Figure 2F, J, Supp video 1). Since the brains were scanned as semi-hemispheres to obtain maximal resolution, it was difficult to trace where these tracts ended. Strikingly, most of the tracts traced to other regions and a large

number extended to the rostroventral brain, which appears to be the anterior visual cortex (remains unannotated in the pig) and many LEC fibers ended in a slightly caudal location to the MEC fibers (Supp Video 1). To sum, the connectivity between the EC and hippocampus in the postnatal pig brain was remarkably similar to that which has previously been reported in other species, including humans (Kolenkiewicz et al., 2009; Mufson et al., 1990; Rowland et al., 2013; Sun et al., 2014; Totterdell and Meredith, 1997; Wilhite et al., 1986; Witter et al., 2017; Witter et al., 1986) which helps to consolidate it as an excellent model for human EC connectivity. We have however, identified a number of potential new locations of EC connectivity that requires further anatomical analysis.

Subheading 2. Cortical lamination of the developing entorhinal cortex is sandwich structured

The timing of birth of pyramidal neurons and stellate cells does not coincide despite the cell's positional proximity. We therefore decided to trace the cortical lamination patterning of the EC and emergence of cell types in detail. To this end, we examined the MEC among developing posterior EC from E23 to P75 (Figure S3A). Since neurogenesis has been poorly studied in the developing pig brain, we first evaluated the timing of neurogenesis. Immunohistochemistry of the MEC was performed at over 8 time points from E23 to P75 of development. Using antibodies directed against GFAP, FABP7 (BLBP), SOX2 and PAX6, we assessed the presence of neural epithelium (NE) (PAX6+/FABP7-) at E23 and radial glia (GFAP+/FABP7+) at E26, and we also measured the size of the ventricular zone (VZ) (PAX6+) (Figure S3B-D). We identified that the VZ is already well-established by E23 and that it peaked in size at E50, whereby it then declined dramatically in size at E60 (Figure S3C, D). We then investigated the second germinal zone by performing histochemistry using EOMES and PAX6 specific antibodies. Our results showed the presence of a moderately sized layer containing diffuse numbers of EOMES+ during neurogenesis. This diffuse layer, known as the outer subventricular zone (OSVZ), is extensive in size in humans and non-human primates, but smaller in ferrets and rats (Fietz et al., 2010; Martinez-Cerdeno et al., 2012; Smart et al., 2002). Assessment and quantification of the cell type proportion and population, respectively showed that EOMES+/PAX6+ and EOMES+/PAX6- SVZ showed equal ratio of population at E26 (Figure S3E, F). At E33, two distinct layers could be observed above the VZ, a dense inner subventricular zone (ISVZ) containing equal proportions of EOMES+/PAX6+ and EOMES+/PAX6- cells and a diffuse overlying zone, the OSVZ, containing EOMES+/PAX6+ and EOMES+/PAX6- cells. We observed that the ratio between EOMES+/PAX6+ and EOMES+/PAX6- population changed over time, with EOMES+/PAX6+ becoming more abundant in both the ISVZ and OSVZ (Figure S3E, F), when the distinct morphology was declined at E70. The OSVZ remained moderate in size. Considering PAX6 is an important transcriptional regulator of neurogenesis, with increasing expression changing the balance from neural stem cell renewal to neurogenesis (Sansom et al., 2009), our findings implying that neurogenesis might occur from E33 until shortly after E60.

Analysis of cortical lamination was performed using immunohistochemical analyses of canonical markers for deep (CTIP2/BCL11B) and superficial layers (SATB2), as well as EOMES, RELN and TBR1 across varying times of gestation. During early cortical formation (E21) we detected the presence of EOMES+ and RELN+ cells towards the pial surface. Co-expression of EOMES+/RELN+ cells were detected 2 days later at E23 and expression of TBR1 emerged in some of these cells at E23 with more RELN+/TBR1+ cells detectable by E33 (Figure S3G, H). We believe these cells to be migrating and maturing Cajal–Retzius cells (CR cells), which are important for the cortical lamination process (Hevner et al., 2003). We then traced the emergence of local neurons using BCL11B and SATB2. As expected, BCL11B was the first of the two markers to be expressed at E33 and was located in the cortical plate (Figure S4A). Interestingly, a large proportion of the BCL11B+ cells expressing SATB2 in the cytoplasm could be detected in the superficial layer at E39 (Figure S4A). This co-expression could also be detected in the dorsal telencephalon, but at an earlier stage at E33 (Figure S4A), suggesting a timeline of neurogenesis in different areas of the cortex. By E50 a distinct new population of BCL11B cells had emerged at the superficial layer of the EC which could not be observed in the dorsal telencephalon (Figure 3A, B). These large prominent nuclei resemble the prominent large entorhinal cells that were observed histologically (Figure S2). In the dorsal telencephalon, a SATB2+ population emerged in the superficial layer at E50 which remained present until gestation (Figure 3A, B) which was not detected in the EC. In contrast, in the EC, a new population of BCL11B positive cells emerges at E60 which does not lie over the superficial large nuclei BCL11B population. This indicates that the EC does not form in an inside out lamination pattern, but the latest born neurons form LIII instead of LII neurons. This positioning is retained until after birth (Figure 3C) and is not noted in the dorsal telencephalon (Figure 3B). As the *lamina dissecans* develops, the SATB2+ neurons originally found at the superficial layer at E33 form the LV. A small proportion of the LII BCL11B+ cells began to express RELN at E60 with expression becoming more abundant in the superficial cells at E70 (Figure 3B, C). The RELN+ neurons residing in both the MEC and LEC continued to express BCL11B until after birth (Figure 3D, E). Collectively, our findings suggested that the superficial neurons of the EC arise from the fourth wave of lamination and that the fifth wave of lamination forms LIII. We therefore conclude that lamination patterning in the EC differs remarkably from neighbouring areas of the cortex.

Subheading 3. Single-cell RNA sequencing reveals 32 cell populations in the MEC

Single-cell RNA sequencing (scRNA-seq) is a powerful approach that has led to a deeper understanding of the molecular identity of several cell types in varying brain regions. We used this methodology to investigate the timing in the emergence of different cell types of the EC and their molecular identity during development and in the postnatal brain. We performed scRNA-seq using the 10X Genomics microfluidics based Chromium platform on whole-cells isolated from the EC at E50, E60, E70 and P75, and isolated nuclei in the later stages of development at E70 and P75 to ensure efficient capture of the neurons in the tissue (Figure 4A). Downstream clustering and

data analysis was performed in Seurat v2 (Satija et al., 2015) (Figure 4A). We excluded red blood cells (expressing hemoglobin subunits *HBB, HBE1, HBM, HBZ* and on average, only 291 genes per cell) and vascular cells (*PDGFRB*$^{+}$/*PECAM1*$^{+}$) from our dataset which left us with 24,294 cells. Confident in our data, we then performed cell clustering and detected 32 distinct cell clusters (Figure 4B). The clusters could be delineated into 6 main cell populations demarcated by canonical markers for IPs, excitatory neurons, inhibitory interneurons (IN), microglia, oligodendroglia (Oligo), and glial cells, which included both astrocytes (*AQP4*$^{+}$/*GFAP*$^{+}$/*GLAST*$^{+}$) and radial glia (*HES1*$^{+}$/*SOX2*$^{+}$) (Figure 4C). One cluster, namely cluster 30, contained a small number of cells (n=70) which contained twice as many transcripts and genes expressed (Figure 4C) which we believed to be doublets and which failed to be removed by the data-preprocessing. This cluster was not included in further analyses. Furthermore, we validated our marker-expression driven annotations by projecting our dataset using scmap (Kiselev et al., 2018) onto a publicly available and annotated dataset of the human embryonic prefrontal cortex (Zhong et al., 2018) and an unpublished dataset from the human adult middle temporal gyrus (Bioarchive, https://doi.org/10.1101/384826) (Figure 4E). We found a high concordance between our annotation and the human brain datasets, despite the obvious regional differences, with two exceptions. A discrepancy was observed in the annotation of clusters 2 and 25. We initially identified these as INs, however, the scmap projection annotated these two clusters as excitatory neurons (Figure 4C, E). Despite the scmap annotation of cluster 25 as excitatory neurons, their expression profile related to that of IN with expression of GAD1/2 and absence in expression of vGLUT1/2. For cluster 2, a closer analysis of canonical markers suggests an ambiguous identity, mainly at E60, expressing both the excitatory markers vGLUT1/2 and the IN markers GAD1/2 (Figure 4B, C). The UMI counts for this cluster were normal, meaning it is unlikely to be a doublet cluster and might suggest a unique and ambiguous progenitor cell type in the EC. Our confidence in the dataset allowed us to progress in assessing the glia and neuron populations to further analyse the genotypes of the EC cells. Distinguishing subtypes of specific cell types based on the entire population using Seurat is difficult. Therefore, subclustering and subsequent analyses were performed on the oligodendroglia (Figure 5), excitatory neurons and IPs (Figure 5), and IN clusters (Figure 6) to elucidate new cell types within these discrete subpopulations.

Subheading 4. Single-cell RNA sequencing analysis reveals OPCs emerge in the EC at E50.

We characterized the transcriptome of the predominant population of OLIG2+ OPCs found in the superficial layers of the LEC (Figure 1D-E, S2D-E). Subclustering and analysis of the oligodendroglia clusters 3, 12, 24, 27 (Figure 5A insert) revealed 5 distinct populations (Figure 5A, B). Cluster 30, which grouped with the oligodendrocytes and expressed *MBP* (Figure 4), was omitted from the sub-analysis, as the highest enriched genes in this cluster were found to be mitochondrial genes (Figure S5A) and they are likely to be dying cells. Two clusters (OPC1 and 2) expressed the oligodendrocyte precursor lineage and early oligodendrocyte markers

PDGFRA and *OLIG1* (Figure 5C), with a large proportion of the cells undergoing cell cycle division (50% and 25% respectively, Figure 5D). We were unable to identify *OLIG2* in these two clusters, likely due to low copy numbers and subsequent gene dropout effects. However, this data suggested these two clusters were progenitor cells. Cluster OPC1 was composed of fetal cells from E50 to E70 whilst cluster OPC0 also contained adult cells (Figure 5B). We therefore believe that cluster OPC1 emerges earlier during development and corresponds to the first wave of oligodendrogenesis. We believe these to be two separate populations of OPCs, with one remaining present until after birth and the other differentiating into pre-myelinating oligodendrocytes (and changing their transcriptional profile). To characterize whether these clusters resided in spatially different niches, we further examined their unique gene signatures (Figure 5C). Cluster OPC0 expressed the genes *LHFPL3* and *MMP16*, and cluster OPC1, *STMN1*. These genes have been previously identified in OPCs (Artegiani et al., 2017; Hu et al., 2011; Lin et al., 2009; Magri et al., 2014). Interestingly, we found the OPC0 marker *CNTN1* to be expressed in the superficial layers in the developing mouse EC (Figure 5E, from the Allen Brain Atlas (Lein et al., 2007)). We believe that the OPC0 population represents the unique population of OPCs identified histologically in the superficial layers of the LEC (Figure 1D-E). Interestingly, our data revealed an additional population which constituted of fetal cells from mainly E60; OLI2 (Figure 5A-B). These cells expressed more mature oligodendrocyte markers including, *MBP*, *CLDN11*, *GRP17*, *NKX2-2*, and *MAG* (Figure 5C). OLI2 cells expressed high levels of *FYN*, predominantly in the upper layers of the developing E18.5 mouse EC. Together, this data suggests that a small population of myelinating oligodendrocytes is apparent already in the fetal porcine EC. The oligodendrocyte clusters OLI3 and OLI4 consisted almost exclusively of adult cells and were highly similar in profile (Figure 5B, C). We speculated these were mature myelinating oligodendrocytes. They differed in proliferation as nearly all OLI3 cells expressed G2M/S-phase cycling genes while OLI4 cells were mostly quiescent and expression genes from the G0/1-phase of the cell cycle (Figure 5D). The OLI3 unique gene marker, *OXR1,* was expressed in LI-III of the adult mouse EC while the OLI4 unique gene marker, *DLG2*, was found in the deep layers (Figure 5E-F). In summary, our data indicate the presence of 2 OPC populations that reside in different layers of the EC, one pre-myelinating oligodendrocyte population and two similar mature oligodendrocyte profiles.

Subheading 5. Single-cell RNA sequencing reveals unique gene signatures for stellate cells and pyramidal neuron populations

To gain a deeper understanding of the temporal pattern of emerging neurons we performed subclustering on the IP and excitatory neuron populations identified from the parent dataset and uncovered unique gene expression signatures. We subclustered and analyzed a total of 7,672 cells, including the excitatory clusters 0, 5, 10, 15, and 17 and IP clusters 19, 21, 22, and 23 (Figure 6A, insert). The subclustering revealed 13 distinct populations (Figure 6A). Cells from the gestational stages dominated the subset of IPs and excitatory neurons, with only very few adult cells included (Figure 6B). This is likely due to the overall fewer cells captured in the

postnatal brain samples. Amongst the clusters, one population pertained a typical IP identity. Herein, cells in cluster IP4 expressed the typical IP markers *EOMES, SOX2*, and *NEUROD4* (Figure 6C) (Pollen et al., 2015) and could be detected across all stages of development (Figure 5B).

An analysis of canonical genes for immature neurons with a pyramidal-like identity revealed several potential cell populations. Clusters PYR1, PYR0, PYR2, PYR3 and PYR12 were tangentially located on the t-SNE plot (Figure 6A) and co-expressed *NRP1* (Figure 6C), which is reportedly expressed in pyramidal precursor cells and downregulated in mature pyramidal neurons (Sano et al., 2017). Surprisingly, we did not observe any neuron populations expressing *CALB1*, a common pyramidal neuron marker reported in rats, mice and humans within the EC (Beall and Lewis, 1992; Diekmann et al., 1994; Fujimaru and Kosaka, 1996). Further analysis of immunohistochemical labelled EC did reveal expression of CALB1 in the adult EC and only limited expression at E100 (Figure S2A), with no expression detectable at earlier stages. Similarly, in the mouse brain, a few CALB1 positive cells are present in the EC at E18.5, while at P4 CALB1 is widely expressed in the EC (Allen Brain Institute, developmental ISH atlas), suggesting that CALB1 is not expressed in the fetal EC. Clusters PYR0 and PYR1 shared similar transcriptional profiles but had divergent *NEUROD1* expression. Clusters PYR2 and PYR3 were also remarkably similar, but had divergent *ARPP21* expression. We found cluster PYR12 to be an intriguing population. It had an overlapping profile of both the PYR0, PYR1 and PYR2, PYR3 clusters, suggestive of an immature pyramidal neuron, however, it also expressed the more mature pyramidal neuron marker *EMX1* (Chan et al., 2001) and a moderate level of *RELN* (Figure 6C) (a marker for the stellate cell) (Perez-Garcia et al., 2001). Additionally, this cluster also had low expression of the interneuron markers *DLX1/5* (Figure 6C) and *GAD1/2* (data not shown). Further investigations are required to assess the identity of cluster PYR12. We believe we have captured the profile of at least 2 young pyramidal neuron populations, since it is difficult to separate PYR0 from PYR1 and to separate PYR2 from PYR3. We are confident in this, since these populations were captured across all gestational ages (Figure 6B). We additionally captured a young neuron population with both an excitatory and inhibitory identity (PYR12). This population of cells with a unique ambiguous transcriptional identity has not been reported previously and likely belongs to one of the unique cell types found in the EC, requiring further investigation.

An analysis of mature pyramidal neuron markers revealed several potential populations, of which two overlapped with a precursor identity. Clusters PYR2, PYR3, and PYR7 expressed *EMX1* and the excitatory marker neuron marker *vGLUT2* (Figure 6C). Cluster PYR6 expressed the pyramidal neuron marker *TBR1* (Englund et al., 2005) and shared a similar gene signature profile to that of cluster PYR7 (Figure 6C). Given the tangential shapes of clusters PYR1, PYR0, and PYR2, PYR3 and PYR7, PYR6 and the tangential change of immature to mixed immature/mature to mature transcriptional identity it is tempting to speculate the transitional emergence of a single pyramidal neuron. However, the gene signature profiles of clusters PYR0, PYR1 were remarkably similar to each other, as was clusters PYR2, PYR3 and clusters PYR6, PYR7 and all were present across several gestational ages. Most interestingly,

clusters PYR0, PYR2 and PYR6 were only present in the postnatal brain and therefore we deduce to have captured 3 pyramidal neuron profiles of immature (clusters PYR1, PYR3, PYR7) identity and mature (clusters PYR0, PYR2, and PYR6) identity. Validation of two unique gene markers in the Allen Brain Atlas corroborated the putative location of these cells. The gene *TNR* is highly expressed in PYR2 and PYR3 and was found in the superficial layers of the mouse EC. The gene *NEUROD6* was highly upregulated in PYR2, PYR3 and PYR6, and PYR7 clusters and can be detected in both the superficial and deeper layers, suggesting that clusters PYR6 and PYR7 may reside both in the superficial and deeper layers or deeper layers alone. Taken together, we believe that we have identified three pyramidal neuron types in the EC with unique spatial location.

In addition to the pyramidal neurons, the EC harbors two types of principal neurons expressing RELN, the stellate and fan cells, residing in LII/III in the MEC and LEC, respectively (Witter et al., 2017). Our subclustering analysis revealed 4 distinct excitatory neuron populations that expressed *RELN*. Apart from the known expression of RELN and absence of CALB1, few other genes are known to be expressed in these cells (Fuchs et al., 2016; Kitamura et al., 2014; Winterer et al., 2017). The clusters RELN5, RELN8, RELN10, RELN11 expressed *RELN* and lacked the pyramidal transcription factor, *EMX1* (Figure 6C). Cluster RELN8 and RELN11 separated distinctly on the t-SNE plot and had distinct gene signatures to the remaining clusters (Figure 6C). In particular, cluster RELN11 was different from cluster STE8, since nearly all cells were in either G2M or S-phase, while the majority of cells in cluster RELN8 were in G1-phase (Figure S5B). Both clusters could only be detected during neurogenesis (E50 and E60), therefore we believe these to be young RELN positive neurons of different identities. In the E18.5 mouse EC, a unique marker for the RELN11 cluster, *CXCR4*, was expressed across all the layers (Figure 6D). The other two clusters STE5 and STE10 were expressed throughout all ages and persisted in the postnatal adult brain (Figure 6B). They had quite distinct transcriptional profiles and separated far from each other on the t-SNE plot (Figure 6A-C). We could not identify the location of RELN5 neurons using the mouse brain atlas and the markers that were uniquely found in our dataset, therefore we cannot deduce the location of these neurons. Cluster RELN10, expressed moderate levels of RELN and also expressed the marker gene *CPNE4*, which is expressed in the superficial layers of the mouse EC and more enriched in the LEC than the MEC LII (Figure 6B-D). Nearly all cells in the cluster were found to be in G1/G0-phase of cell-cycle (Figure S5B). Further, *EPHA6* which was upregulated in cluster RELN10 could be observed in the LII-LIII in the adult mouse brain, confirming the likely location of the RELN10 neurons, to be in the superficial layer. We believe cluster RELN10 represents either the adult stellate and/or fan cell genotype.

Interestingly, we identified a unique population which did not fit either stellate or pyramidal cell expression profiles, cluster SPE9. This population was negative for *vGLUT* and *SST* expression, but expressed *RELN,* and *GAD1/2*. Therefore, we identified a unique expression profile for this population (Figure 6C). Expression of *SFRP2*, one of the cluster-specific genes, is found not only in the superficial layers of the EC, but across all the layers in adult mice, and across both the MEC and LEC

(Figure 6D). We found that most cells were undergoing cell-cycle division, while the other part of the cluster were in G1/G0-phase (Figure S5B). This suggests that the cluster included both progenitors and mature states of the cell type. Together, these findings concur with current knowledge on speed cells, known to be GABAergic, absent for SST expression and present across all layers of the EC (Kropff et al., 2015; Ye et al., 2018), although marker expression suggests this cell type is equally present in the LEC. Since no other population expressed this combination of markers, we believe we have identified this unique cell type in the EC and provide a unique gene signature for this cell including *SFRP2, COL2A1, COL18A1, SIX3* and *SIX6*.

To further verify that the excitatory neuron cell types we identified from the pig EC are representative of EC cells in other species, we projected our IP and excitatory neuron dataset onto a recently published scRNA-seq dataset of the developing entire brain from P2 and P11 mice which included 156,049 single nuclei transcriptomes (Rosenberg et al., 2018) (Figure S6A-B). The projection showed that our pyramidal clusters matched closely with the mouse cortical and hippocampal pyramidal neurons identified from the Rosenberg dataset. Our remaining neuron clusters matched less well to the data set. The RELN clusters were more heterogeneous in nature, with no strong matches to any single cluster and the SPE9 cluster matched closest with hippocampal pyramidal neurons and cerebellar granule precursors. We believe the sequencing depth of the Rosenberg dataset may not be detailed enough to identify the EC specific neuron clusters, but it helps to verify using a whole brain dataset from a different species that our excitatory neuron populations, albeit unique, contain pyramidal, glutamatergic neurons.

Subheading 6 Three somatostatin positive and three somatostatin negative interneuron populations are detected in the entorhinal cortex

To gain a better understanding of the temporal pattern of emerging INs within the EC, we sub-clustered a total of 2,942 cells from the dataset which expressed canonical IN markers *DLX1, GAD1* and *GAD2* (clusters 2, 25, 18 and 16). The subclustering identified 7 clusters (IN0-IN6, Figure 7A). The proportion of cells from different developmental ages within each cluster can be seen in Figure 7B. We evaluated these clusters for the expression of several well-known canonical IN markers including *CALB1*, *CALB2*, *DLX5*, *GAD1, GAD2, GATA3, LHX1*, *LHX5*, *LHX6*, *NPY, RELN SST*, *TACR1* (Figure 7C) and *HTR3A, PVALB*, *CCK*, *NOS1*, LHX5, and *VIP*, although these latter genes could not be identified in the scRNA-seq dataset, likely due to low expression. Of these latter markers, *PVALB* has been particularly important for the identification of INs in the EC. Several references have reported PVALB+ INs and their inhibitory gradients in the EC (Beed et al., 2013; Fujimaru and Kosaka, 1996; Miao et al., 2017; Willems et al., 2018; Wouterlood et al., 1995). To confirm that PVALB was expressed at low levels during early gestation, we performed immunohistochemistry and detected moderate PVALB+ in the superficial layers from E100 (Figure 7G) and onwards (P75) (Figure S2A).

We then identified unique transcriptional signatures for each cluster (Figure 7D). The IN0-IN2 populations expressed *SST,* whereas the IN3-IN6 populations were absent for *SST* (Figure 7C). Immunolabeling of the EC brain revealed high expression of *SST* across all the EC layers at E60 (Figure 7F). IN0 and IN1 had relatively similar transcriptional profiles, with some notable small transcriptional differences. IN0 had higher *SST* expression and lower expression of *RELN.* IN0 also expressed *GAD2* (Figure 7C). Both clusters uniquely expressed a gene, *SNCB*, which was identified across LII to LVI in the adult mouse brain. Another gene, *RESP18* was more highly expressed in IN1 and was localized to the superficial layers and deep layers (Figure 7E), suggesting IN1 is not found in the middle layers. However, given the relative similarities of expression between IN0 and IN1 (Figure 7D), it cannot be concluded that IN0 and IN1 are separate cell populations. The other IN populations appeared more transcriptionally unique. The IN2 population was captured across all time points and had high expression of *RELN* (Figure 7B,C). Expression of the GABAB receptor subunit gene *KCTD8* is highly upregulated in IN2 and is expressed across all the layers in the adult mouse brain (Figure 7E) suggesting the IN2 population is distributed across all layers of the EC. IN3 uniquely expressed *LHX6* and *CORT*. Expression of *CORT* in the mouse adult brain is also found across all EC layers suggesting distribution of IN3 throughout (Figure 7E,G). The IN4 population uniquely expressed *GATA3* whilst the IN5 population expressed high levels of *DLX5* (Figure 7E). GATA2 and 3 have been found in unique ventral IN subpopulations in the developing chick, which supports the existence of this ventral population (Karunaratne et al., 2002). Similarly, DLX5 is an important regulator of PVALB-expression (Wang et al., 2010). The IN6 population was only detected during embryonic gestation at E50 and E60 (Figure 7B), suggestive of a progenitor IN population. This population also clustered furthest from the remaining clusters (Figure 7A) and expressed high levels of *NDNF.* We could detect *NDNF* in LI and in deeper layers in the E18.5 mouse EC (Figure 7G) highlighting the putative location of these INs during development. In sum, we identified three SST+ and three SST- IN populations in the EC, of which 1 population is only present during development.

Discussion

We have classified the staging of neurogenesis in a large mammalian model, the pig, which we have found an excellent choice for studying brain development and which mirrors the temporal timing of human neurogenesis. Given it is extremely difficult to obtain human fetal tissue during the second and third trimester, the large gyrencephalic pig brain has proved to be a very good alternative model. Neurogenesis spans from E39 to E60 in the ventral telencephalon of the pig (during the 1st and early 2nd trimester), which corresponds more closely to the timing of neurogenesis within the human cortex (gestational week 7-17) (Kostovic et al., 2019) than to mice (E11-E17) (Casarosa et al., 1999; Roy et al., 2004; Stagni et al., 2015). The anatomical orientation of the pig EC was also similar to that in the developing human brain. To view the six-layered EC in the rodents, sagittal sectioning is required, whereas, we could better view the EC in the pig in the coronal plane, similar to the situation in the human. Immunohistochemical analyses across development resulted in the detection of a moderate OSVZ during E33-E60 with a

change in proportion of intermediate progenitors with mixed identity of EOMES+/PAX6- and EOMES+/PAX6+ to an enriched number of EOMES+/PAX6+ cells. Considering that PAX6 is an important transcriptional regulator of neurogenesis with increasing expression changing the balance from neural stem cell renewal to neurogenesis, (Sansom et al., 2009), we believe that neurogenesis lasts from E39 until shortly after E60. We have discovered that the pig has a larger OSVZ than rodents and that the timing of neurogenesis concurs with trimester matched neurogenesis in the human.

During gestation, entorhinal cells become visible already at E50 (during the early second trimester) and the EC becomes multilayered by E60, comprising key cytoarchitectonic features delineating the MEC from the LEC. Early emergence of the EC in humans occurs towards the end of the first trimester with prominent entorhinal cells visible by 10.5 weeks post ovulation (Kostovic et al., 1993), which is thus closely aligned between these two species. In the rat, the entorhinal cells emerge later, at E16 (Deng et al., 2006), and in the mouse, stellate cells (RELN+) emerge by E12, with pyramidal neurons emerging approximately 2 days later (Donato et al., 2017). In our study, we found the superficial BCL11B+ entorhinal cells emerged at E50 and BCL11B+/RELN+ cells could be detected from E60 onwards, indicating a gap in birth and expression of maturing neurons within the superficial layers. Together, our study highlights that the pig shares temporal similarities in the developing EC to the human.

The EC emerges in a sandwich lamination pattern with LII neurons born early during neurogenesis. Maturation of the MEC has been described recently as dorsoventral in the mouse, which correlates with the birth of the stellate cells, but not with the pyramidal neurons (Donato et al., 2017). We extend this data to show that LII superficial neurons (we do not discern between stellate and pyramidal) are born prior to LIII as also reported in Donato et al., and that a sandwich patterning of cortical lamination occurs, which has not been well recognized. This patterning has also been reported in the anatomical classification of the developing EC in the rat, which succinctly shows that LIII forms after LII (Bayer et al., 1993). We concur with this earlier study and supplement the research with labeling of superficial versus deep layer markers, in combination with a temporal analysis of expression across gestation. Our additional analyses show that this altered expression of markers persists until after birth. Bromodeoxyuridine labeling would certainly help uncover the precise emergence of the different layers in the EC and determine whether LIII emerges prior to, or after LV and LIV. However, given the quantities of BrDU required for administration of >200 kg pregnant sows we did not embark on this study. Of particular interest, our data together with ISH data from Allen Brain Atlas indicate diverging expression patterns of BCL11B between mouse and pig brain. An increase of the transcriptional regulator, PAX6 in apical progenitors is important for the generation of superficial cortical neurons (Georgala et al., 2011). Therefore, it is plausible that PAX6 expression levels might differ in the EC versus other regions. It would also be of interest to examine whether altered RELN expression within the local CR cells could affect the lamination patterning. Further research is required to

investigate the signaling mechanisms underlying this unique cortical development feature.

We identified two OLIG2+ OPC populations in the LEC which reside in different layers. The pan-neuronal clustering and abundance of OPCs in the LEC concurs with the particular enrichment of projections we observed in the DTI from the LEC's superficial projection neurons. The early emergence of these OPCs during gestation suggests that at least one wave of oligodendrogenesis overlaps with EC neurogenesis. In mice, the first OPCs emerge from the ventral medial ganglionic eminence at E11.5 and migrate throughout the telencephalon in a ventral to dorsal manner midway through gestation (Kessaris et al., 2006), which is only slightly later than what we observe in the pig. One OPC population (OPC1) continued to conserve its OPC signature until after birth, whereas another population (OPC0) residing in the superficial layers lost its identity later during gestation, likely due to transitioning to a more mature phenotype (potentially OLI2). The remaining OPC population residing in the EC even after birth is an interesting population. Research has previously indicated that OPCs can give rise to pyramidal neurons in the piriform cortex in the adult mouse (Guo et al., 2010). Such plasticity has not been described in the EC, however it would be interesting to trace the fate of these cells in the adult EC and evaluate EC plasticity. The pre-myelinating oligodendrocyte phenotype (OLI2) expressed *MBP* and emerged quite early during gestation, at E60, which indicates myelination begins much earlier in the pig than previously thought. A previous study has shown myelination of white fibers in 2 month old pigs (Fang et al., 2005) but our study suggests the myelination process may occur much earlier in the pig cortex. Together, we highlight the presence of two OPC populations that reside in spatially different locations within the developing EC.

At the single-cell level, we characterized the transcriptome of the developing entorhinal cortex cells including the excitatory neurons, inhibitory neurons, glia and progenitors. The dataset projected extremely well using scmap to human and mouse datasets, which suggests this dataset can be used with confidence. Although, the human datasets were at unmatched gestational ages and from the embryonic prefrontal cortex and adult middle temporal gyrus, only 2 clusters were unable to be projected to them. We were able to identify an IP population within the EC expressing *EOMES, SOX2* and *NEUROD4* and 12 young/adult excitatory neuron profiles, of which include 3 young pyramidal and 3 mature pyramidal neuron types. An additional 4 populations expressing RELN had distinct profiles of which two were expressed only during gestation, whilst two others were expressed even after birth. Many of these clusters have been spatially mapped using their gene-specific signatures to the adult EC. Some clusters exhibited a mixed identity with both an excitatory and inhibitory mixed genotype. We have also discovered the speed cell transcriptional profile. This particular population was negative for vGLUT and SST expression, but expressed *RELN* and *GAD1/2*. Unique markers expressed in the SPE9 cluster included *SFRP2*, a notable WNT Inhibitor (Kongkham et al., 2010) important for axon guidance (Lyuksyutova et al., 2003), COL2A1, important for chondrogenesis (Hering et al., 2014), COL18A1, important in eye development (Fukai et al., 2002), as well as SIX3 and SIX6, which are implicated in retinal and anterior brain development

(Diacou et al., 2018; Lagutin et al., 2003). This unique gene set will be useful for identifying and studying the speed cell in future research. Our research does warrant follow up studies that can match the outlined transcriptomes more precisely to phenotypes, but the spatial dimension provided from tracing unique genes in the mouse brain gives good indications of the cell types to which they belong. For example the identification of subcluster 10, expressed across gestation and in the postnatal brain was the only RELN expressing cluster found postnatally and exclusively located in the superficial layer. We therefore believe that this genotype belongs to the Fan and/or stellate cell. Concurrently, cluster 3 has a pyramidal neuron identity which extended in the postnatal brain and also resides in the superficial layer. Very few gene markers can currently be used to identify the cell types of the EC. Until now, only RELN and CALB1 could be used to decipher stellate cells from pyramidal neurons (Perez-Garcia et al., 2001; Seress et al., 1994). Here, we provide more encompassing gene signatures for a diverse number of detectable excitatory and inhibitory neuron cell populations.

Together, we bring forth a novel animal model for studying brain development which we have used to trace in detail the developing entorhinal cortex. We described a sandwich-structured EC with the LII forming prior to LIII. We have decoded the molecular identity of the cell types in the EC and using spatial mapping of unique genes identified unique gene signatures that together with spatial positioning of unique markers from these signatures, identify the identity of several cell types in the EC. This research helps fill the void of the genetic constitution of the EC cells and further research will be useful for connecting the genotypes to the phenotypes to gain even more precision in the understanding of the functional circuitry of the spatial navigational system.

Acknowledgements:

We thank Per Torp Sangild for his donation of healthy adult sow brains for this study. We acknowledge the Core Facility for Integrated Microscopy, Faculty of Health and Medical Sciences, University of Copenhagen for access and use of the Axio Scan Z.1. We also acknowledge Anna Fossum, FACS Facility at BRIC, University of Copenhagen for help with the sorting. The project was financed by The Independent Research Fund, Denmark under the grant (ID: DFF–7017-00071 and 8021-00048B), Lundbeck fund (R296-2018-2287) and The Innovation Foundation (Brainstem (4108-00008B)), Novo Nordisk Hallas-Møller Investigator grant (NNF16OC0019920). THP acknowledges the Novo Nordisk Foundation (Grant number NNF18CC0034900) and the Lundbeck Foundation (Grant number R190-2014-3904). MH and NP were supported by a core grant to the Wellcome Sanger Institute from the Wellcome Trust. LFH was supported by Open Targets (OTAR038) and JL was supported by a CZI (2018-183503 (5022)) from the Chan Zuckerberg Initiative. We also acknowledge the Single Cell Core Facility at BRIC, University of Copenhagen for access to sc-seq services.

Author Contributions:

Terms used to describe contribution have been sent according to the recommended list: https://www.cell.com/pb/assets/raw/shared/guidelines/CRediT-taxonomy.pdf

YL: Methodology; Investigation; Formal Analysis; Writing –Original Draft, Writing – Review & Editing, Visualization
TB: Methodology; Investigation; Formal Analysis; Writing –Original Draft, Writing – Review & Editing, Visualization
JL: Investigation
UP: Investigation
L-FH: Software
YM: Investigation, Formal Analysis
AAM: Investigation
ILV; Investigation
SES: Investigation, Supervision
JTHL: Software
NP: Software
JMPV: Investigation, Formal Analysis
MP: Investigation
BRK: Resources
PDT: Resources
PH: Resources, Supervision, Funding Acquisition
MPW: Formal Analysis, Funding Acquisition
KK: Resources, Supervision, Methodology
JG: Resources, Supervision
MH: Software, Resources, Supervision
THP: Resources; Formal Analysis; Software
VH: Conceptualization; Methodology; Validation; Formal Analysis; Resources, Writing –Original Draft, Writing –Review & Editing, Visualization, Supervision, Project Administration, Funding Acquisition

Declaration of Interests:
The authors declare no competing interests.

Figure titles and legends

Figure 1. Cytoarchitectonic features of the developing porcine EC. (A) Length and trimester divisions of the gestation in mouse, human, and pig. **(B)** Macroscopic view of the ventral surface of the porcine brain at E100 with annotation of the piriform lobe including the entorhinal area. Olfactory tract (Olf.Tr.); caudate nucleus of amygdala (COA); hippocampal area (HA); lateral entorhinal cortex (LEC); medial entorhinal cortex (MEC); sagittal sulcus (S.Sag); posterior rhinal sulcus (RHP). **(C)** Delineations and cytoarchitectonic features of cresyl violet stained coronal sections

of the EC (shown at E100 as representative). Light grey punctuated line marks the acellular L4 l*amina dissecans*, black punctuated line borders between MEC and LEC or EC and adjacent areas. Red arrows (middle panels) shows the difference in the cellular organization in deep layers, arrowheads highlight large superficial cells of the EC. Medial (M); lateral (L); pre-subiculum (PreS); para-subiculum (PAS), perirhinal cortex (PER); layer 2 - 5 (LII - LV). **(D)** Oligodendroglia-like cells in the superficial layers of the EC and adjacent areas. Neocortex (NEO). High magnification of red squares in **(E)** where the morphology of the oligodendroglia-like cells is demonstrated at E100 (red arrowheads).

Figure 2. Magnetic resonance imaging (MRI) of the developing EC and diffusion tensor imaging (DTI) of the white matter projections shows a spurt in growth during late 2nd trimester and projections to varying brain regions at P75. (A) MRI shows the rostral to caudal position of the early developing EC and postnatal EC in the coronal plane (marked in orange). **(B)** The EC volume shows a particular growth spurt at E70 when compared with cortex volume changes during development. **(C)** An overview of white matter fibers connecting to the MEC (orange) and LEC (purple). **(D)** The average number of tracts connecting to the MEC and LEC do not differ significantly. **(E)** White matter fibers connecting to the perirhinal cortex (triangles) and postrhinal cortex (arrows). **(F)** White matter fibers extend from the EC to the corpus callosum (arrow). **(G)** White matter fibers connecting to the lateral (arrow) and medial olfactory bulb (triangle). **(H)** White matter fibers connecting to the hippocampus (arrow). **(I)** White matter fibers connecting to the amygdala (triangle). **(J)** Average number of tracts connecting to different anatomical regions emerging from the EC do not significantly differ between the MEC and LEC. All error bars denote SD. n.s.p >0.05, * P≤0.05, ** P≤0.01, *** P≤0.001.

Figure 3. Altered expression of superficial and deep layer markers in the EC persists until after birth. (A) Location of analyzed ventral telencephalon (V), MEC, and dorsal telencephalon (D) at E50 and E60 of development. **(B)** Altered expression of superficial layer marker SATB2 and deep layer marker BCL11B in the ventral telencephalon and MEC combined with the expression of RELN compared to the dorsal telencephalon. **(C)** Expression of SATB2, BCL11B, and RELN in the MEC from E70 until P75 of development. **(D)** Location of analyzed superficial layers across the EC, including the MEC and LEC. **(E)** RELN+ neurons co-express BCL11B across the EC during gestation and also after birth. Scale bar 50 µm (B, C) and 25 µm (E).

Figure 4. Single-cell profiling of the EC reveals 32 distinct cell clusters of major cell type populations in the EC. (A) The bioinformatic pipeline includes 10 batches of the whole cell and isolated nuclei cells from E50, E60, E70 and Adult which were captured as single cells using the 10x genomics platform. Batches were normalized using the Fast MNN approach, dimensional reduction and clustering were performed in Seurat and subclustering and analyses of selected clusters was performed. **(B)** A t-SNE plot of 24,294 cells merged from all timepoints revealed 32 distinct populations. **(C)** Analysis of canonical marker genes resulted in categorization of several oligodendro-glia/-cytes (Oligo), astrocytes and radial glia (Glial cells), intermediate

progenitors (IP), excitatory neurons (Excitatory), interneurons (IN) and microglia (Microglia) clusters, together with the number of cells, mean UMI counts and expressed genes for each cluster. Error bars denote SD. **(D)** Batch correction by FastMNN resulted satisfactory merge of the 10 datasets (pre-batch correction shown in Figure S5C). **(E)** Projection of the dataset onto already-annotated human fetal prefrontal cortex and human medial temporal gyrus single-cell dataset consolidates marker gene-driven annotation of the dataset. Blood cells expressing *HBB*.

Figure 5. Oligodendrocytes and precursors in the EC. (A) Visualization of oligodendroglia subset (2,696 cells) in 5 distinct cluster in a t-SNE plot. Subset of the oligodendroglia (orange) within the parent dataset is depicted in the insert in the top left corner. **(B)** Developmental stages of the oligodendroglia visualized in a t-SNE plot. **(C)** Canonical lineage markers and unique gene signatures for the 5 clusters identified by differential gene expression analysis. Localization of genes with names in blue is shown in (E). * human ortholog names (Supp. Table 2). **(D)** Distribution of cells in different cell-cycle phases in the 5 clusters. Notably, G1-phase is indistinguishable from G0-phase of cell-cycle. **(E)** Sagittal sections of murine EC (from Allen Brain Atlas) with ISH staining, of either fetal (E18.5) or adult brain sections.

Figure 6. Molecular diversity of the excitatory neurons and intermediate progenitors of the EC. (A) A t-SNE plot of excitatory neurons and intermediate progenitors (7,627 cells) in 13 distinct clusters. Excitatory neurons (blue) and intermediate progenitors (green) which were subsetted are depicted in insert of the parent dataset. **(B)** Distribution of developmental stages within the 13 clusters. **(C)** Unique gene signatures for the 13 clusters. Localization of genes with names in blue is shown in (D). * human ortholog names (Supp. Table 2). **(D)** Sagittal sections of murine EC (from Allen Brain Atlas) with ISH staining, of either fetal (E18.5) or adult brain sections.

Figure 7. Subclustering of EC interneurons reveals 6 clusters with unique gene signatures. (A) A t-SNE plot of interneurons (IN) forming 7 clusters. **(B)** Distribution of developmental stages within the 7 clusters. **(C)** Expression of canonical IN markers. **(D)** Unique gene signatures identified for the 7 clusters. Localization of genes with names in blue is shown in (F). * human ortholog names (Supp. Table 2). **(E)** SST and BCL11B expression in the MEC. Coronal section of the pig EC at E60. Scale bar 50 µm (left) and 25 µm (right). **(F)** Sagittal sections of mouse E18.5 and adult EC (from Allen Brain Atlas, with ISH staining. Scale bar 200 µm. **(F)** SST and BCL11B expression in the MEC. Coronal section of the pig EC at E60. Scale bar 50 µm (left) and 25 µm (right).

STAR METHODS

CONTACT FOR REAGENT AND RESOURCE SHARING

Further information and requests for resources and reagents may be directed to and will be fulfilled by the Lead Contact, Vanessa Hall (vh@sund.ku.dk).

EXPERIMENTAL MODEL AND SUBJECT DETAILS

Animal welfare and collection of brains

The experiments conform to the relevant regulatory standards for use of fetal material. Crossbred male and female pig fetuses at E26, E33, E39, E50, E60, E70, E80 and E100 of development were obtained from inseminated Danish Landrace/Yorkshire sows with Duroc boar semen from a local pig production farm. Note, the average gestation length for this crossbreed is 114 days. The uteri were removed following the slaughter of the sows by trained and licensed personnel at a local slaughterhouse and transported warm at 37°C to the University where the fetuses (clinically dead from asphyxiation during transport) were then isolated by umbilical excision from their fetal sacs. Deceased postnatal pigs were obtained at P75 as a gift from Per Torp Sangild at the University of Copenhagen. Adult brains were obtained from sows killed for another study using an overdose of sodium phenobarbital by a professional issued with a license from the Danish Animal Experiment Inspectorate.

METHOD DETAILS

Brain Fixation and storage

For the earlier time points up until E60, the entire fetus was fixed and the dorsal skull was opened to improve permeation of the fixative. For the later time points, the brains were removed from the skull. Fixation was performed using 4 % PFA (Millipore Sigma) in PBS (Thermo Fisher Scientific) from 24 hrs to up to 2 weeks, dependent on the size of the fetus/brain. Fetuses and brains were then stored long-term at 4°C in 0.002% Sodium Azide (VWR - Bie&Berntsen) in PBS.

Paraffin embedding and sectioning

Prior to dehydration, the brains were dissected to approximately 10 mm thickness. The brains were dehydrated by immersion into a sequential series of ethanol, estisol and liquid paraffin using a tissue Processor (Thermo Fisher Scientific Citadel 2000). Following dehydration, the tissues were embedded in liquid paraffin followed by cooling down on a cold stage. Five-micrometer (µM) thick sections were cut on a microtome (Leica SM2000R) and mounted onto SuperFrost slides (Thermo Fisher Scientific). The sections were dried at room temperature (RT) overnight (ON) and stored long term at 4° C.

Cresyl Violet Staining

Paraffin embedded sections were deparaffinized for 45 min at 60°C and 2x 10 min in Xylene. The sections were sequentially rehydrated for 2x 5 min in 99% EtOH, 3 min in 96% EtOH, 3 min in 70% EtOH, rinsed in tap water and stained for 12 min in 37°C Cresyl Violet (Millipore Sigma). The stained sections were rinsed in distilled water and staining outside of perikarya was differentiated for 10 min in 96% EtOH with 0.02% glacial acetic acid (Millipore Sigma). The sections were subsequently dehydrated 2x 5 min in 99% EtOH and 2x 5 min in Xylene prior to coverslip mounting using DPX (Sigma-Aldrich). All images were acquired on an Axio Scan.Z1 (Zeiss) using automated brightfield imaging.

Tissue-Tek OCT embedding and Cryosectioning

Fixed fetuses/brains were dehydrated in 30% sucrose(Sigma-Aldrich)/1x PBS (Thermo Fisher Scientific) solution (0.22 µm filtered) at 4°C for 48 hours (h). The brains were cut into small pieces of approximately 4 mm thickness. The brain tissues were immersed into Tissue-Tek OCT (Sakura) and mounted within plastic molds (Simport) by snap-freezing in N-hexane ((VWR) solution immersed within liquid nitrogen. The frozen tissue was stored at -80°C until use. Brain sections were cut at 30 µm thickness using a cryostat (Leica CM 1950) and mounted onto SuperFrost Plus slides (Thermo Fisher Scientific) and stored at -20°C.

Immunohistochemistry

Paraffin embedded brain sections were deparaffinized for 45 min at 60°C in the oven and 2x 10 min in Xylene(VWR). Subsequently, the sections were sequentially rehydrated for 2x 5 min in 99% EtOH, 3 min in 96% EtOH, 3 min in 70% EtOH, 3 min in tap water, and washed 2x for 5 min in PBS. The sections were subsequently permeabilized for 30 min in 0.1% Triton-X (Millipore Sigma) in PBS at RT and washed 2x 5min in PBS before antigen retrieval in boiling citrate [0.01M, pH6] (Sigma-Aldrich) for 3x 5 min. The sections were washed once for 5 min in PBS and Lab Vision™ MultiVision Polymer Detection System (Thermo Fisher Scientific) was used according to manufacturer's protocol with the following specifications: Anti-parvalbumin (Millipore Sigma) primary antibody was diluted in 1:500 in PBS and incubated at RT for 30 min. The sections were visualized with LVRed and LVBlue.

Immunofluorescence

Cryosectioned brains were air-dried for 1hr at RT, followed by rehydration in PBS (Thermo Fisher Scientific) for 10 min. After the antigen retrieval (detailed description at Immunohistochemistry staining) the sections were permeabilized in 0.25% Triton X-100/PBS (Sigma-Aldrich) for 10 minutes followed by washing in PBS. The brain tissue was demarcated with a hydrophobic pen followed by blocking in the

blocking buffer which contain 10% Normal donkey serum (Biowest) 2% BSA (Sigma-Aldrich) at RT for 1 h. The sections were then incubated with the diluted primary antibody (see below) ON at 4°C followed by washing in PBS 3 times for 5 mins each. The sections were then incubated in diluted secondary antibody for 2h at RT and thereafter washed in PBS for 3 times for 5 mins each. The sections were counterstained with 10 µg/ml Hoechst 33258 (Sigma-Aldrich) for 10 min followed by washing in PBS for 5 mins twice. Finally, the sections were mounted with a glass coverslip in fluorescence mounting medium (DAKO). The primary antibodies and secondary antibodies were diluted with blocking buffer. The primary antibodies used are as the source table. Different antibodies combinations were applied to the same sections during individual reactions according to the proteins under study. Secondary antibodies were diluted at 1:200 and selected to be the same species as the species used for producing the primary antibodies and were conjugated with either Alexa fluorophores, 488, 594 or 647.

Image processing and quantification

For acquisition of Cresyl Violet images, a bright-field microscope, Leica DMR with camera Leica DFC490 and Zeiss Axio scan.Z1 were used to capture the images. For acquisition of immunohistochemistry images, a confocal microscope Leica TCS SPE was used. Samples belonging to the same experiment (samples from experimental pig at a given time point, with their controls) were acquired in parallel and with the same settings (laser power: 8-20%; optical slice: 1 airy units, step size: 3 µm for population analysis) using 40×/1.15 oil immersion objective . Prior to the acquisition, gain and digital offset were established on sections from secondary antibody control sample to optimize the dynamic range of acquisition to the dynamic range of the staining (baselines were set independently for every staining based on the protein under investigation). Settings were kept constant during acquisition. Confocal images were acquired using Leica LAS X. Images were optimized for brightness and contrast using Fiji-ImageJ. Statistical analysis was conducted with commercially available software- Prism 7.0 (GraphPad Software).

Structural MRI

A 9.4T BioSpec 94/30 USR spectrometer (Bruker BioSpin, Ettlingen, Germany) equipped with a 240 mT/m gradient system was used to acquire anatomical images of postmortem porcine brains (E60, E70, E80, E100, P75). Prior to imaging, the PFA fixed brain were suspended into plastic containers filled with a proton-free perfluorinated susceptibility-matching fluid (Solvay Galden® HT-230). We used a 35-mm (for P75) and a 23-mm (for E60, E70, E80, and E100) inner diameter transmit/receive volume coil (Bruker). The MR system was interfaced to a console running ParaVision software 6.0.1 (Bruker BioSpin). The parameters used in the brain scans were optimized for gray/white matter contrast: T2-weighted 2D rapid acquisition with relaxation enhancement (RARE) pulse sequence with TR/TE = 20000/40 ms (before birth), 12000/60 ms (after birth), Rare factor = 8 (before birth), 16 (after birth), in-plane resolution = 100 µm × 100 µm, slice thickness = 200

µm (before birth), 500 µm (after birth). 3D fast low angle shot (3D-FLASH) pulse sequence with TR/TE = 30/4.6 ms, Flip angle = 10, NA = 16, spatial resolution = 47 µm × 47 µm × 70 µm. The total imaging time was 2 hours.

Diffusion MRI tractography

Ex vivo diffusion tensor imaging (DTI) of P75 brain (n = 3) was obtained using a Stejskal-Tanner sequence (TR/TE = 3500/17.5ms, NA = 2, spatial resolution = 390 µm × 390 µm × 390 µm) on a 9.4T spectrometer equipped with a 1500 mT/m gradient system and a 40-mm inner diameter transmit/receive volume coil. We applied the motion probing gradients (MPGs) in 60 noncollinear directions with b = 2500 s/mm^2 in addition to 4 b0. Diffusion Toolkit (version 0.6.4.1) and TrackVis (version 0.6.1) were used for 3D reconstruction of white matter tracts. We used a DWI mask threshold and an angular threshold of 45 degrees. Two regions of interest (ROIs) were selected a priori for the DTI analysis: including the LEC and MEC. ROIs were created by manually segmentation with ITK-snap (version 3.6.0, (Yushkevich et al., 2006)). The fiber tracks obtained from the ROIs were qualitatively analyzed for the direction of tracks, and differences in FA values within the brain parenchyma. The assessment was done using tractography maps: (1) a standard color-coded reconstruction to visualize the orientation of tracks where blue tracks represented diffusion in the craniocaudal direction, green tracks represented diffusion in the anterior-posterior direction, and red tracks showed diffusion in the transverse direction; (2) a scalar FA map with minimum and maximum FA thresholds of 0.1 and 0.6, respectively; and (3) total track length information for each ROI.

Single-cell preparation

In total we prepared 10 sequencing-libraries form isolated MECs from E50 (whole cell, 3 brains, 1 batch), E60 (whole cell, 4 brains, 3 batches), E70 (whole cell, 4 brains, 3 batches; nucleus 1 brain, one batch) and from adult sow MEC (whole cell, 1 brain, 1 batch; nucleus, 1 brain, 1 batch) (Table S1). Briefly, the individual MEC tissue was digested using a papain dissociation method, according to the manufacturer's guidelines (Worthington) with small modifications.

The EC was macroscopically dissected out (approx. 1 mm^3) in the digest medium (1x PBS (Thermo Fisher Scientific), 1x Penicillin-Streptomycin (Sigma-Aldrich)), transferred to a 3.5cm Petri dish and incubated in 1mL papain solution for 30 min at 37°C. Solution and remaining tissue were subsequently transferred to a 15 mL falcon and gently triturated 20 times. The cell suspension was diluted with 1 mL FBS (BioWest) and centrifuged for 5 min at 300 g, RT. The supernatant was discarded and the cell pellet was resuspended in prepared solution with 2.7 mL digestion media (1x Neurobasal medium (Thermo Fisher Scientific), 10% FBS (BioWest), 1x Penicillin-Streptomycin (Sigma-Aldrich)), 300 uL albumin-ovomucoid inhibitor, and 150 uL DNAse solution. The cell suspension was carefully layered on top of 5.0 ml of albumin-inhibitor solution in a 15 mL falcon tube and centrifuged for 6 min at 70 g, RT. The supernatant was discarded and the cell pellet was resuspended in 5 mL cell-

resuspension media (1x Neurobasal medium (Thermo Fisher Scientific), B27 (Thermo Fisher Scientific), 1x Penicillin-Streptomycin (Sigma-Aldrich), bFGF (5 ng/ml, Prospec). The cells were counted (NucleoCounter, ChemoMetec) and diluted to 100-2000 cells/uL used for single-cell library preparation.

Single nuclei isolation

Nuclei extraction was performed as described before with the following modifications (Krishnaswami et al., 2016). Prior to nuclei extraction, nuclei isolation medium 1 (NIM1) (250 mM sucrose, 25 mM KCl, 5 mM MgCl2, 10 mM Tris Buffer pH8), NIM2 (NIM1 buffer supplemented with 1 µM DTT (Thermo Fisher Scientific) and 1x EDTA-free protease inhibitors (Roche) and homogenization (NIM2 buffer supplemented with Recombinant RNase Inhibitor (0.4 U/µL, Takara), SUPERase in (0.2 U/µL, Thermo Fisher Scientific) and Triton (0.1% v/v, Sigma-Aldrich)) buffers were prepared. Briefly, sectioned frozen brain tissue was placed into pre-cooled 1ml dounce homogenizer (Wheaton) with 1ml ice-cooled homogenization buffer. Tissue was dissociated on ice using 5-6 strokes with the loose pestle and 15-17 strokes with the tight pestle. Homogenate was first filtered through a 70 µm filter. Nuclei were collected (900 g, 10 min) and resuspended in 500µl staining buffer (nuclease free PBS (1X, Thermo Fisher Scientific), BSA (0.5% wt/vol, Sigma-Aldrich), SUPERase in (0.2 U/µL, Thermo Fisher Scientific)). Then the sample was stained by the 7-AAD (2µg/ml, Sigma-Aldrich) followed by FACS sorting (70 µm nozzle, BD Biosciences, BD FACSAria™) to 1.5ml eppendorf tube contained with 10 µl 10% nuclease free BSA (Thermo Fisher Scientific).

Single Cell/Nuclei RNA-seq library preparation and sequencing

The whole cells were loaded onto the 10X Genomics microfluidic chip according to the Chromium Single Cell 3' Reagent Kits User Guide (10X Genomics) following adequate dilution. The single nuclei samples were loaded onto the 10X Genomics microfluidic chip similarly, albeit the samples were not diluted. 10-12.000 thousand cells/nuclei were loaded from each sample.

Libraries from two samples at different stages were pooled and sequenced together on an Illumina NextSeq 500 (Table S1) following the NextSeq System Denature and Dilute Libraries Guide Protocol A: Standard Normalization Method (illumina). The NextSeq 500/550 High Output Reagent Cartridge v2 75 cycles (illumina) kit was used for the whole cell and single nuclei samples and the pooled library were sequenced on NextSeq 500. The sequencing cycles were: Read1, 26 cycles, i7 Index 8 cycles, i5 Index 0 cycles; Read2, 57 cycles.

QUANTIFICATION AND STATISTICAL ANALYSIS

Statistics:

For immunohistochemistry and assessement of neuroconnectivity from DTI white matter tracts, all samples were performed in biological triplicates. Statistical analysis was conducted using commercially available software- Prism 7.0 (GraphPad Software). Dependent on the experimental design, an ordinary one-way ANOVA or an unpaired two-tailed t test was performed to statistically assess differences. All error bars denote SD. n.s.p >0.05, * P≤0.05, ** P≤0.01, *** P≤0.001.

Initial quality control and data analysis

Briefly, the sequenced libraries were mapped to pre-mRNA and filtered using 10X Genomics Cell Ranger pipeline.

The sequencing data was demultiplexed by bcl2fast (illumina) which warped in the Cell Ranger followed by aligning to reference genome (Sscrofa11.1 release-94) by STAR (Dobin et al., 2013). Finally, mRNA molecules were counted and by Cell Ranger. The quality of the sequencing libraries was assessed by Cell Ranger, which determined in each sample the sequencing depth cutoff that is required for cells to be included in the downstream analysis. Similar number of UMIs and genes were observed across all batches (Figure S5D-E).

Batch correction

We used decomposeVar from the 'scran' R package (RRID: SCR_001905) in order to find a list of variable genes that are used for PCA dimensionality reduction; however, to aid the correspondence of single cell to single nucleus, we identified and excluded genes whose transcripts were highly abundant in empty droplets (cells with <50 UMIs). If the number transcripts that are found in the empty droplet is above 30% the total number of transcripts for a given gene (Figure S5F), that gene will be removed from the list of variable genes.

The projected gene expression was then batch corrected by FastMNN (Haghverdi et al., 2018), which reduced the distance between cell pairs that are found to be reciprocally nearest neighbors across batches (before batch correction; Figure S5C, after correction; Figure 4B). The merged dataset were visualized by t-distributed stochastic neighbour embedding (t-SNE) (van der Maaten and Hinton, 2008).

Unsupervised clustering and cell type identification

Cell types were identified using the Louvain algorithm with a resolution parameter set at 1.6 for all clustering analyses. The canonical markers were used to identify the neurons of the clusters (Figure 4C). In addition, we used two reference datasets

which each contained smart-seq2 single-cells from human embryonic prefrontal cortex (Fan et al., 2018; Zhong et al., 2018) or from human adult middle temporal gyrus (Astick and Vanderhaeghen, 2018). We used Scmap (Kiselev et al., 2018) to project individual cells onto curated cell-type clusters that are available in each reference. Each cell-type prediction utilize the consensus of 3 similarity measures from queried cell to reference cluster centroids using sets of cell-type markers that were identified in the respective reference datasets; however, only the human genes that possess an ortholog gene in pig were used as cell type marker for similarity measure calculation.

Differential gene expression analysis

For cluster cj, gene gi is considered a true positive (TP) if it is expressed, a false negative (FN) if it is not expressed, a false positive (FP) if is expressed in a cell assigned to another cluster, and a true negative (TN) if it is not expressed in a cell assigned to a different cluster. For each gi we evaluate precision = TP/(TP+FP), recall = TP/(TP+FN), and F1 = 2*precision*recall/(precision + recall). For each cj, genes are ranked by F1 with the highest scoring genes used as markers.

For analysis of enriched genes in the oligodendroglia population (Figure 5C) these were found using Seurats function FindAllMarkers, with wilcoxon rank sum test used and only considering genes expressed in at least 25% of the cells in either of the tested populations. The 5 most highly enriched genes are reported here.

Cell-cycle score analysis

Cell-cycle phases were scored using the built in function in Seurat CellCycleScoring, which was used to determine whether a given cell was likely to be in either S, G2M or G1 (which is indistinguishable from G0) phase of cell-cycle. Cell-cycle scores were based on a list of cell-cycle phase-specific genes proposed by Tirosh et al. (Tirosh et al., 2016).

DATA AND SOFTWARE AVAILABILITY

Data availability

The data is publically available at NCBI with GEO accession number GSE134482. The submitted data includes the raw sequencing data as fastq files together with the processed count matrix used in this study. The data is also uploaded to Mendeley https://data.mendeley.com/datasets/5fgznjfrzn/draft?a=071f733a-d5e4-424f-a211-d2e9467435bf

Code availability

github

SUPPLEMENTAL INFORMATION

Supplemental Information includes six figures, three tables, and one video and can be found with this article online at..

SUPPLEMENTAL INFORMATION TITLES AND LEGENDS

Figure S1. Borders of the developing porcine entorhinal cortex (EC). Cresyl violet stained coronal sections of the piriform lobe from E60 to P75. The first section rostral to the EC, the second section with LEC occupying the EC entity, third section both MEC and LEC present, fourth section MEC occupies entire mediolateral entity, fifth section very caudal part of the piriform lobe. Dentate gyrus (DG); hippocampal area (HA); amygdala (Amyg); posterior rhinal sulcus (RHP); medial entorhinal cortex (MEC); lateral entorhinal cortex (LEC); pre-subiculum (PreS); para-subiculum (PAS), subiculum (Sub); perirhinal cortex (PER). Scale bar 1 cm.

Figure S2. Validation of delineation of the EC by parvalbumin (PVALB) staining and location and expression of OLIG2 oligodendrocyte progenitor cells. (A) Cresyl violet (from Figure S1) and PVALB expression in the caudal EC at E100 and P75 (coronal plane). **(B)** Cresyl violet staining of glia-like cells at E50 to E70, visible as small round dark stained cells **(C)** Coronal section of E50 brain through the ventral telencephalon destined to become the EC. High magnification of the ventral telencephalon (redbox) shows large superficial cells (arrowheads). **(D)** OLIG2 expression in the developing EC. Images taken in the developing cortical plate (E50-E60), and later (E70-P75), in the superficial layers. **(E)** Quantification of OLIG2 positive cells in the EC by layers/zones. Cortical plate, CP; intermediate zone, IZ; marginal zone, MZ; subplate, SP; subventricular zone, SVZ ventricular zone, VZ. All error bars represent SD.

Figure S3. Characterization of the germinal layer in the porcine EC. (A) Schematic overview of the location characterized. **(B)** Expression of GFAP and FABP7 in the ventricular zone (VZ). Scale bar 25 µm. **(C)** Temporal expression of radial glia (GFAP, FABP7, PAX6, SOX2) during gestation. Scale bar 50 µm **(D).** Quantification of the thickness in µm of the VZ during gestation. **(E)** Expression of EOMES and PAX6 in the EC. Scale bar 25 µm (up) and 50µm (bottom). **(F)** Quantification of the EOMES+/PAX6+ and EOMES+/PAX6- cell populations in the germinal zone. **(G)** TBR1/EOMES expression during gestation. Scale bar 50 µm. **(H)** Expression of TBR1/EOMES in the marginal zone and the cortical plate of (F). Scale bar 25 µm. (HO = Hoeschst, V = ventral telencephalon). Error bars represent SD.

Figure S4. Comparative expression of superficial and deep layer markers in the EC versus the dorsal, cingulate gyrus. Expression of the canonical deep layer marker (BCL11B), superficial layer marker (SATB2) and stellate cell / Cajal–Retzius cells (CR cells) by expression of RELN in the EC and rhinal cortex of the telencephalon. Scale bar 50 µm.

Figure S5. Validation of single-cell sequencing data. (A) Top 10 gene features of cluster 32 found by seurat (FindAllMarkers with wilcoxon) from the scRNA-seq data**.** **(B)** Cell-cycle analysis of IP and excitatory neuron subpopulations (from Figure 5). The cell-cycle score was assessed based on the expression of cell-cycle phase-specific genes. G1 phase of cell-cycle in the analysis is indistinguishable from G0. **(C)** A t-SNE plot of the sc-seq data set prior to fastMNN batch correction. **(D)** Violin plot of the number of UMIs and genes in each single-cell sequencing batch. **(E)** A scatter plot numbers of UMIs versus genes for each batch. **(F)** Fraction of transcripts out of total transcripts for a given gene in empty droplets at representative stages (E70 and Adult), for both isolated nuclei and whole cell samples. Genes with a fraction above 0.30 is not included as variable genes in downstream analysis.

Figure S6. Projection of a mouse P2 and P11 whole-brain dataset resulted in a high degree of matching of cell types on the excitatory neurons and intermediate progenitors of the EC. (A) t-SNE plot of the excitatory neurons and intermediate progenitors of the EC after projection. Original clustering (from Figure 6A) represented by dotted lines. **(B)** Distribution of projected cell-types in the excitatory neurons and intermediate progenitors clusters. Top 3 cell-types in each cluster were labeled with corresponding numbers to the projected data set, see panel A for legend.

Supplementary Tables

Supplementary Table 1. Connectivity of neuronal tracts to/from the lateral and medial entorhinal cortex.

	Total Tracts	MEC	LEC	AM	CA1	CA3	DG	PUT	SUB	LOT	Caudate nucleus	Nucleus accumbens	CC	Other
MEC %	6205.0	-	106.0 (1.71)	730.3 (11.77)	91.3 (1.47)	49.3 (0.79)	47.0 (0.76)	4.7 (0.08)	534.0 (8.61)	3.3 (0.05)	9.0 (0.15)	1.0 (0.02)	11.7 (0.19)	4617.3 (74.41)
LEC %	4516.3	106.0 (2.35)	-	468.7 (10.38)	5.3 (0.12)	10.0 (0.22)	2.7 (0.06)	59.0 (1.31)	1.0 (0.02)	14.3 (0.32)	75.3 (1.67)	0 (0)	0 (0)	3774.0 (83.56)

Average is shown (n=3) and standard deviation in brackets.
AM, amygdala, CC, Corpus collosum; DG, dentate gyrus; LEC, lateral entorhinal cortex; LOT, lateral olfactory tract; MEC, medial entorhinal cortex; PUT, putamen; SUB, subiculum

Supplementary Table 2. Human ortholog gene names identified from pig ensemble names using GeneCard (www.genecards.org).

Ensemble Name	Human ortholog names
ENSSSCG00000010212	ANK3
ENSSSCG00000011178	CPNE4

ENSSSCG00000015545	GLUL
ENSSSCG00000009327	HMGB1
ENSSSCG00000035712	KCTD8
ENSSSCG00000011267	MOBP
ENSSSCG00000015401	PCLO
ENSSSCG00000007644	PILRB
ENSSSCG00000016219	RESP18
ENSSSCG00000033734	TMSB4X
ENSSSCG00000037477	TTC37
ENSSSCG00000029160	UNPROT1
ENSSSCG00000006963	UNPROT2
ENSSSCG00000032935	UNPROT3
ENSSSCG00000037927	UNPROT4
ENSSSCG00000017019	UNPROT5
ENSSSCG00000038101	UNPROT6
ENSSSCG00000036306	UNPROT7
ENSSSCG00000034554	UNPROT8
ENSSSCG00000035520	UNPROT9
ENSSSCG00000036465	USP6NL
ENSSSCG00000005658	ZDHHCL2

Supplementary Table 3. Overview of batches, captured cells, mean reads, numbers of libraries and numbers of brains for sc-seq experiments.

Batch	Estimated Number of Cells	Mean Reads per Cell	Median Genes per Cell	Number of Reads	Library	Brain numbers
E50_1	5506	49042	3448	270029135	2	3
E60_1	8171	27580	2129	225357492	3	1
E60_2	3479	68619	2548	238726637	4	1
E60_3	2696	98734	3335	266189304	1	2
E70_nc	858	305266	1584	261918893	5	1
E70_1	493	599954	4125	295777496	3	1
E70_2	617	484686	3927	299051391	2	1
E70_3	3120	80781	2990	252038762	1	2
Adult_nc	2552	90774	560	231655848	5	1
Adult_1	737	389148	3214	286802165	4	1

Total	28229					

References

Artegiani, B., Lyubimova, A., Muraro, M., van Es, J.H., van Oudenaarden, A., and Clevers, H. (2017). A Single-Cell RNA Sequencing Study Reveals Cellular and Molecular Dynamics of the Hippocampal Neurogenic Niche. Cell Rep *21*, 3271-3284.

Astick, M., and Vanderhaeghen, P. (2018). From Human Pluripotent Stem Cells to Cortical Circuits. Curr Top Dev Biol *129*, 67-98.

Bayer, S.A., Altman, J., Russo, R.J., and Zhang, X. (1993). Timetables of neurogenesis in the human brain based on experimentally determined patterns in the rat. Neurotoxicology *14*, 83-144.

Beall, M.J., and Lewis, D.A. (1992). Heterogeneity of layer II neurons in human entorhinal cortex. J Comp Neurol *321*, 241-266.

Beed, P., Gundlfinger, A., Schneiderbauer, S., Song, J., Bohm, C., Burgalossi, A., Brecht, M., Vida, I., and Schmitz, D. (2013). Inhibitory gradient along the dorsoventral axis in the medial entorhinal cortex. Neuron *79*, 1197-1207.

Bergmann, E., Zur, G., Bershadsky, G., and Kahn, I. (2016). The Organization of Mouse and Human Cortico-Hippocampal Networks Estimated by Intrinsic Functional Connectivity. Cereb Cortex *26*, 4497-4512.

Bjarkam, C.R., Glud, A.N., Orlowski, D., Sorensen, J.C.H., and Palomero-Gallagher, N. (2017). The telencephalon of the Gottingen minipig, cytoarchitecture and cortical surface anatomy. Brain Struct Funct *222*, 2093-2114.

Bjerknes, T.L., Langston, R.F., Kruge, I.U., Moser, E.I., and Moser, M.B. (2015). Coherence among head direction cells before eye opening in rat pups. Curr Biol *25*, 103-108.

Bjerknes, T.L., Moser, E.I., and Moser, M.B. (2014). Representation of geometric borders in the developing rat. Neuron *82*, 71-78.

Burwell, R.D., and Amaral, D.G. (1998). Perirhinal and postrhinal cortices of the rat: interconnectivity and connections with the entorhinal cortex. J Comp Neurol *391*, 293-321.

Canto, C.B., and Witter, M.P. (2012a). Cellular properties of principal neurons in the rat entorhinal cortex. I. The lateral entorhinal cortex. Hippocampus *22*, 1256-1276.

Canto, C.B., and Witter, M.P. (2012b). Cellular properties of principal neurons in the rat entorhinal cortex. II. The medial entorhinal cortex. Hippocampus *22*, 1277-1299.

Canto, C.B., Wouterlood, F.G., and Witter, M.P. (2008). What does the anatomical organization of the entorhinal cortex tell us? Neural Plast *2008*, 381243.

Casarosa, S., Fode, C., and Guillemot, F. (1999). Mash1 regulates neurogenesis in the ventral telencephalon. Development *126*, 525-534.

Chan, C.H., Godinho, L.N., Thomaidou, D., Tan, S.S., Gulisano, M., and Parnavelas, J.G. (2001). Emx1 is a marker for pyramidal neurons of the cerebral cortex. Cereb Cortex *11*, 1191-1198.

Conrad, M.S., Dilger, R.N., and Johnson, R.W. (2012). Brain growth of the domestic pig (Sus scrofa) from 2 to 24 weeks of age: a longitudinal MRI study. Dev Neurosci *34*, 291-298.
Conrad, M.S., Sutton, B.P., Dilger, R.N., and Johnson, R.W. (2014). An in vivo three-dimensional magnetic resonance imaging-based averaged brain collection of the neonatal piglet (Sus scrofa). PLoS One *9*, e107650.
Deng, J.B., Yu, D.M., and Li, M.S. (2006). Formation of the entorhino-hippocampal pathway: a tracing study in vitro and in vivo. Neurosci Bull *22*, 305-314.
Diacou, R., Zhao, Y., Zheng, D., Cvekl, A., and Liu, W. (2018). Six3 and Six6 Are Jointly Required for the Maintenance of Multipotent Retinal Progenitors through Both Positive and Negative Regulation. Cell Rep *25*, 2510-2523 e2514.
Diekmann, S., Nitsch, R., and Ohm, T.G. (1994). The organotypic entorhinal-hippocampal complex slice culture of adolescent rats. A model to study transcellular changes in a circuit particularly vulnerable in neurodegenerative disorders. J Neural Transm Suppl *44*, 61-71.
Dobin, A., Davis, C.A., Schlesinger, F., Drenkow, J., Zaleski, C., Jha, S., Batut, P., Chaisson, M., and Gingeras, T.R. (2013). STAR: ultrafast universal RNA-seq aligner. Bioinformatics *29*, 15-21.
Domnisoru, C., Kinkhabwala, A.A., and Tank, D.W. (2013). Membrane potential dynamics of grid cells. Nature *495*, 199-204.
Donato, F., Jacobsen, R.I., Moser, M.B., and Moser, E.I. (2017). Stellate cells drive maturation of the entorhinal-hippocampal circuit. Science *355*.
Englund, C., Fink, A., Lau, C., Pham, D., Daza, R.A., Bulfone, A., Kowalczyk, T., and Hevner, R.F. (2005). Pax6, Tbr2, and Tbr1 are expressed sequentially by radial glia, intermediate progenitor cells, and postmitotic neurons in developing neocortex. J Neurosci *25*, 247-251.
Fan, X., Dong, J., Zhong, S., Wei, Y., Wu, Q., Yan, L., Yong, J., Sun, L., Wang, X., Zhao, Y.*, et al.* (2018). Spatial transcriptomic survey of human embryonic cerebral cortex by single-cell RNA-seq analysis. Cell Res *28*, 730-745.
Fang, M., Li, J., Gong, X., Antonio, G., Lee, F., Kwong, W.H., Wai, S.M., and Yew, D.T. (2005). Myelination of the pig's brain: a correlated MRI and histological study. Neurosignals *14*, 102-108.
Farr, M., Kitas, G.D., Waterhouse, L., Jubb, R., Felix-Davies, D., and Bacon, P.A. (1988). Treatment of psoriatic arthritis with sulphasalazine: a one year open study. Clin Rheumatol *7*, 372-377.
Fietz, S.A., Kelava, I., Vogt, J., Wilsch-Brauninger, M., Stenzel, D., Fish, J.L., Corbeil, D., Riehn, A., Distler, W., Nitsch, R.*, et al.* (2010). OSVZ progenitors of human and ferret neocortex are epithelial-like and expand by integrin signaling. Nat Neurosci *13*, 690-699.
Fuchs, E.C., Neitz, A., Pinna, R., Melzer, S., Caputi, A., and Monyer, H. (2016). Local and Distant Input Controlling Excitation in Layer II of the Medial Entorhinal Cortex. Neuron *89*, 194-208.
Fujimaru, Y., and Kosaka, T. (1996). The distribution of two calcium binding proteins, calbindin D-28K and parvalbumin, in the entorhinal cortex of the adult mouse. Neurosci Res *24*, 329-343.

Fukai, N., Eklund, L., Marneros, A.G., Oh, S.P., Keene, D.R., Tamarkin, L., Niemela, M., Ilves, M., Li, E., Pihlajaniemi, T.*, et al.* (2002). Lack of collagen XVIII/endostatin results in eye abnormalities. EMBO J *21*, 1535-1544.
Garcia-Cabezas, M.A., John, Y.J., Barbas, H., and Zikopoulos, B. (2016). Distinction of Neurons, Glia and Endothelial Cells in the Cerebral Cortex: An Algorithm Based on Cytological Features. Front Neuroanat *10*, 107.
Gatome, C.W., Slomianka, L., Lipp, H.P., and Amrein, I. (2010). Number estimates of neuronal phenotypes in layer II of the medial entorhinal cortex of rat and mouse. Neuroscience *170*, 156-165.
Georgala, P.A., Manuel, M., and Price, D.J. (2011). The generation of superficial cortical layers is regulated by levels of the transcription factor Pax6. Cereb Cortex *21*, 81-94.
Germroth, P., Schwerdtfeger, W.K., and Buhl, E.H. (1989). Morphology of identified entorhinal neurons projecting to the hippocampus. A light microscopical study combining retrograde tracing and intracellular injection. Neuroscience *30*, 683-691.
Giocomo, L.M., Stensola, T., Bonnevie, T., Van Cauter, T., Moser, M.B., and Moser, E.I. (2014). Topography of head direction cells in medial entorhinal cortex. Curr Biol *24*, 252-262.
Guo, F., Maeda, Y., Ma, J., Xu, J., Horiuchi, M., Miers, L., Vaccarino, F., and Pleasure, D. (2010). Pyramidal neurons are generated from oligodendroglial progenitor cells in adult piriform cortex. J Neurosci *30*, 12036-12049.
Haghverdi, L., Lun, A.T.L., Morgan, M.D., and Marioni, J.C. (2018). Batch effects in single-cell RNA-sequencing data are corrected by matching mutual nearest neighbors. Nat Biotechnol *36*, 421-427.
Hering, T.M., Wirthlin, L., Ravindran, S., and McAlinden, A. (2014). Changes in type II procollagen isoform expression during chondrogenesis by disruption of an alternative 5' splice site within Col2a1 exon 2. Matrix Biol *36*, 51-63.
Hevner, R.F., Neogi, T., Englund, C., Daza, R.A., and Fink, A. (2003). Cajal-Retzius cells in the mouse: transcription factors, neurotransmitters, and birthdays suggest a pallial origin. Brain Res Dev Brain Res *141*, 39-53.
Holm, I.E., and Geneser, F.A. (1989). Histochemical demonstration of zinc in the hippocampal region of the domestic pig: I. Entorhinal area, parasubiculum, and presubiculum. J Comp Neurol *287*, 145-163.
Hu, J.G., Wang, Y.X., Zhou, J.S., Chen, C.J., Wang, F.C., Li, X.W., and Lu, H.Z. (2011). Differential gene expression in oligodendrocyte progenitor cells, oligodendrocytes and type II astrocytes. Tohoku J Exp Med *223*, 161-176.
Insausti, R., Herrero, M.T., and Witter, M.P. (1997). Entorhinal cortex of the rat: cytoarchitectonic subdivisions and the origin and distribution of cortical efferents. Hippocampus *7*, 146-183.
Insausti, R., Tunon, T., Sobreviela, T., Insausti, A.M., and Gonzalo, L.M. (1995). The human entorhinal cortex: a cytoarchitectonic analysis. J Comp Neurol *355*, 171-198.
Jelsing, J., Nielsen, R., Olsen, A.K., Grand, N., Hemmingsen, R., and Pakkenberg, B. (2006). The postnatal development of neocortical neurons and glial cells in the Gottingen minipig and the domestic pig brain. J Exp Biol *209*, 1454-1462.
Karunaratne, A., Hargrave, M., Poh, A., and Yamada, T. (2002). GATA proteins identify a novel ventral interneuron subclass in the developing chick spinal cord. Dev Biol *249*, 30-43.

Kessaris, N., Fogarty, M., Iannarelli, P., Grist, M., Wegner, M., and Richardson, W.D. (2006). Competing waves of oligodendrocytes in the forebrain and postnatal elimination of an embryonic lineage. Nat Neurosci *9*, 173-179.
Kim, S.W. (2010). Recent advances in sow nutrition. Revista Brasileira de Zootecnia *39*, 303-310.
Kiselev, V.Y., Yiu, A., and Hemberg, M. (2018). scmap: projection of single-cell RNA-seq data across data sets. Nat Methods *15*, 359-362.
Kitamura, T., Pignatelli, M., Suh, J., Kohara, K., Yoshiki, A., Abe, K., and Tonegawa, S. (2014). Island cells control temporal association memory. Science *343*, 896-901.
Kolenkiewicz, M., Robak, A., Rowniak, M., Bogus-Nowakowska, K., Calka, J., and Majewski, M. (2009). Distribution of cocaine- and amphetamine-regulated transcript in the hippocampal formation of the guinea pig and domestic pig. Folia Morphol (Warsz) *68*, 23-31.
Kongkham, P.N., Northcott, P.A., Croul, S.E., Smith, C.A., Taylor, M.D., and Rutka, J.T. (2010). The SFRP family of WNT inhibitors function as novel tumor suppressor genes epigenetically silenced in medulloblastoma. Oncogene *29*, 3017-3024.
Kostovic, I., Petanjek, Z., and Judas, M. (1993). Early areal differentiation of the human cerebral cortex: entorhinal area. Hippocampus *3*, 447-458.
Kostovic, I., Sedmak, G., and Judas, M. (2019). Neural histology and neurogenesis of the human fetal and infant brain. Neuroimage *188*, 743-773.
Krishnaswami, S.R., Grindberg, R.V., Novotny, M., Venepally, P., Lacar, B., Bhutani, K., Linker, S.B., Pham, S., Erwin, J.A., Miller, J.A.*, et al.* (2016). Using single nuclei for RNA-seq to capture the transcriptome of postmortem neurons. Nat Protoc *11*, 499-524.
Kropff, E., Carmichael, J.E., Moser, M.B., and Moser, E.I. (2015). Speed cells in the medial entorhinal cortex. Nature *523*, 419-424.
Lagutin, O.V., Zhu, C.C., Kobayashi, D., Topczewski, J., Shimamura, K., Puelles, L., Russell, H.R., McKinnon, P.J., Solnica-Krezel, L., and Oliver, G. (2003). Six3 repression of Wnt signaling in the anterior neuroectoderm is essential for vertebrate forebrain development. Genes Dev *17*, 368-379.
Langston, R.F., Ainge, J.A., Couey, J.J., Canto, C.B., Bjerknes, T.L., Witter, M.P., Moser, E.I., and Moser, M.B. (2010). Development of the spatial representation system in the rat. Science *328*, 1576-1580.
Lein, E.S., Hawrylycz, M.J., Ao, N., Ayres, M., Bensinger, A., Bernard, A., Boe, A.F., Boguski, M.S., Brockway, K.S., Byrnes, E.J.*, et al.* (2007). Genome-wide atlas of gene expression in the adult mouse brain. Nature *445*, 168-176.
Leitner, F.C., Melzer, S., Lutcke, H., Pinna, R., Seeburg, P.H., Helmchen, F., and Monyer, H. (2016). Spatially segregated feedforward and feedback neurons support differential odor processing in the lateral entorhinal cortex. Nat Neurosci *19*, 935-944.
Lin, G., Mela, A., Guilfoyle, E.M., and Goldman, J.E. (2009). Neonatal and adult O4(+) oligodendrocyte lineage cells display different growth factor responses and different gene expression patterns. J Neurosci Res *87*, 3390-3402.
Lyuksyutova, A.I., Lu, C.C., Milanesio, N., King, L.A., Guo, N., Wang, Y., Nathans, J., Tessier-Lavigne, M., and Zou, Y. (2003). Anterior-posterior guidance of commissural axons by Wnt-frizzled signaling. Science *302*, 1984-1988.

Magri, L., Gacias, M., Wu, M., Swiss, V.A., Janssen, W.G., and Casaccia, P. (2014). c-Myc-dependent transcriptional regulation of cell cycle and nucleosomal histones during oligodendrocyte differentiation. Neuroscience *276*, 72-86.
Martinez-Cerdeno, V., Cunningham, C.L., Camacho, J., Antczak, J.L., Prakash, A.N., Cziep, M.E., Walker, A.I., and Noctor, S.C. (2012). Comparative analysis of the subventricular zone in rat, ferret and macaque: evidence for an outer subventricular zone in rodents. PLoS One *7*, e30178.
Miao, C., Cao, Q., Moser, M.B., and Moser, E.I. (2017). Parvalbumin and Somatostatin Interneurons Control Different Space-Coding Networks in the Medial Entorhinal Cortex. Cell *171*, 507-521 e517.
Mufson, E.J., Brady, D.R., and Kordower, J.H. (1990). Tracing neuronal connections in postmortem human hippocampal complex with the carbocyanine dye DiI. Neurobiol Aging *11*, 649-653.
Nilssen, E.S., Jacobsen, B., Fjeld, G., Nair, R.R., Blankvoort, S., Kentros, C., and Witter, M.P. (2018). Inhibitory Connectivity Dominates the Fan Cell Network in Layer II of Lateral Entorhinal Cortex. J Neurosci *38*, 9712-9727.
Olton, D.S., Walker, J.A., and Wolf, W.A. (1982). A disconnection analysis of hippocampal function. Brain Res *233*, 241-253.
Patten, A.R., Fontaine, C.J., and Christie, B.R. (2014). A comparison of the different animal models of fetal alcohol spectrum disorders and their use in studying complex behaviors. Front Pediatr *2*, 93.
Perez-Garcia, C.G., Gonzalez-Delgado, F.J., Suarez-Sola, M.L., Castro-Fuentes, R., Martin-Trujillo, J.M., Ferres-Torres, R., and Meyer, G. (2001). Reelin-immunoreactive neurons in the adult vertebrate pallium. J Chem Neuroanat *21*, 41-51.
Pollen, A.A., Nowakowski, T.J., Chen, J., Retallack, H., Sandoval-Espinosa, C., Nicholas, C.R., Shuga, J., Liu, S.J., Oldham, M.C., Diaz, A.*, et al.* (2015). Molecular identity of human outer radial glia during cortical development. Cell *163*, 55-67.
Pontelo, T.P., Miranda, J.R., Felix, M.A.R., Pereira, B.A., da Silva, W.E., Avelar, G.F., Mariano, F., Guimaraes, G.C., and Zangeronimo, M.G. (2018). Histological characteristics of the gonads of pig fetuses and their relationship with fetal anatomical measurements. Res Vet Sci *117*, 28-36.
Quirk, G.J., Muller, R.U., Kubie, J.L., and Ranck, J.B., Jr. (1992). The positional firing properties of medial entorhinal neurons: description and comparison with hippocampal place cells. J Neurosci *12*, 1945-1963.
Ray, S., and Brecht, M. (2016). Structural development and dorsoventral maturation of the medial entorhinal cortex. Elife *5*, e13343.
Ridley, R.M., Samson, N.A., Baker, H.F., and Johnson, J.A. (1988). Visuospatial learning impairment following lesion of the cholinergic projection to the hippocampus. Brain Res *456*, 71-87.
Rosenberg, A.B., Roco, C.M., Muscat, R.A., Kuchina, A., Sample, P., Yao, Z., Graybuck, L.T., Peeler, D.J., Mukherjee, S., Chen, W.*, et al.* (2018). Single-cell profiling of the developing mouse brain and spinal cord with split-pool barcoding. Science *360*, 176-182.
Rowland, D.C., Obenhaus, H.A., Skytoen, E.R., Zhang, Q., Kentros, C.G., Moser, E.I., and Moser, M.B. (2018). Functional properties of stellate cells in medial entorhinal cortex layer II. Elife *7*.

Rowland, D.C., Weible, A.P., Wickersham, I.R., Wu, H., Mayford, M., Witter, M.P., and Kentros, C.G. (2013). Transgenically targeted rabies virus demonstrates a major monosynaptic projection from hippocampal area CA2 to medial entorhinal layer II neurons. J Neurosci *33*, 14889-14898.
Roy, K., Kuznicki, K., Wu, Q., Sun, Z., Bock, D., Schutz, G., Vranich, N., and Monaghan, A.P. (2004). The Tlx gene regulates the timing of neurogenesis in the cortex. J Neurosci *24*, 8333-8345.
Saikali, S., Meurice, P., Sauleau, P., Eliat, P.A., Bellaud, P., Randuineau, G., Verin, M., and Malbert, C.H. (2010). A three-dimensional digital segmented and deformable brain atlas of the domestic pig. J Neurosci Methods *192*, 102-109.
Sano, N., Shimogawa, T., Sakaguchi, H., Ioroi, Y., Miyawaki, Y., Morizane, A., Miyamoto, S., and Takahashi, J. (2017). Enhanced Axonal Extension of Subcortical Projection Neurons Isolated from Murine Embryonic Cortex using Neuropilin-1. Front Cell Neurosci *11*, 123.
Sansom, S.N., Griffiths, D.S., Faedo, A., Kleinjan, D.J., Ruan, Y., Smith, J., van Heyningen, V., Rubenstein, J.L., and Livesey, F.J. (2009). The level of the transcription factor Pax6 is essential for controlling the balance between neural stem cell self-renewal and neurogenesis. PLoS Genet *5*, e1000511.
Sargolini, F., Fyhn, M., Hafting, T., McNaughton, B.L., Witter, M.P., Moser, M.B., and Moser, E.I. (2006). Conjunctive representation of position, direction, and velocity in entorhinal cortex. Science *312*, 758-762.
Satija, R., Farrell, J.A., Gennert, D., Schier, A.F., and Regev, A. (2015). Spatial reconstruction of single-cell gene expression data. Nat Biotechnol *33*, 495-502.
Schmidt-Hieber, C., and Hausser, M. (2013). Cellular mechanisms of spatial navigation in the medial entorhinal cortex. Nat Neurosci *16*, 325-331.
Seress, L., Leranth, C., and Frotscher, M. (1994). Distribution of calbindin D28k immunoreactive cells and fibers in the monkey hippocampus, subicular complex and entorhinal cortex. A light and electron microscopic study. J Hirnforsch *35*, 473-486.
Smart, I.H., Dehay, C., Giroud, P., Berland, M., and Kennedy, H. (2002). Unique morphological features of the proliferative zones and postmitotic compartments of the neural epithelium giving rise to striate and extrastriate cortex in the monkey. Cereb Cortex *12*, 37-53.
Solstad, T., Boccara, C.N., Kropff, E., Moser, M.B., and Moser, E.I. (2008). Representation of geometric borders in the entorhinal cortex. Science *322*, 1865-1868.
Stagni, F., Giacomini, A., Guidi, S., Ciani, E., and Bartesaghi, R. (2015). Timing of therapies for Down syndrome: the sooner, the better. Front Behav Neurosci *9*, 265.
Stensola, T., and Moser, E.I. (2016). Grid Cells and Spatial Maps in Entorhinal Cortex and Hippocampus. In Micro-, Meso- and Macro-Dynamics of the Brain, G. Buzsaki, and Y. Christen, eds. (Cham (CH)), pp. 59-80.
Sun, L., Wang, J., Liu, H., Fan, Z., Wang, S., and Du, J. (2017). A Comprehensive Study of Palate Development in Miniature Pig. Anat Rec (Hoboken) *300*, 1409-1419.
Sun, Y., Nguyen, A.Q., Nguyen, J.P., Le, L., Saur, D., Choi, J., Callaway, E.M., and Xu, X. (2014). Cell-type-specific circuit connectivity of hippocampal CA1 revealed through Cre-dependent rabies tracing. Cell Rep *7*, 269-280.

Tang, Q., Burgalossi, A., Ebbesen, C.L., Ray, S., Naumann, R., Schmidt, H., Spicher, D., and Brecht, M. (2014). Pyramidal and stellate cell specificity of grid and border representations in layer 2 of medial entorhinal cortex. Neuron *84*, 1191-1197.
Taube, J.S., Muller, R.U., and Ranck, J.B., Jr. (1990). Head-direction cells recorded from the postsubiculum in freely moving rats. II. Effects of environmental manipulations. J Neurosci *10*, 436-447.
Tirosh, I., Izar, B., Prakadan, S.M., Wadsworth, M.H., 2nd, Treacy, D., Trombetta, J.J., Rotem, A., Rodman, C., Lian, C., Murphy, G.*, et al.* (2016). Dissecting the multicellular ecosystem of metastatic melanoma by single-cell RNA-seq. Science *352*, 189-196.
Totterdell, S., and Meredith, G.E. (1997). Topographical organization of projections from the entorhinal cortex to the striatum of the rat. Neuroscience *78*, 715-729.
van der Maaten, L., and Hinton, G. (2008). Visualizing data using t-SNE. Journal of Machine Learning Research *9*, 2579-2605.
Varga, C., Lee, S.Y., and Soltesz, I. (2010). Target-selective GABAergic control of entorhinal cortex output. Nat Neurosci *13*, 822-824.
Wang, Y., Dye, C.A., Sohal, V., Long, J.E., Estrada, R.C., Roztocil, T., Lufkin, T., Deisseroth, K., Baraban, S.C., and Rubenstein, J.L. (2010). Dlx5 and Dlx6 regulate the development of parvalbumin-expressing cortical interneurons. J Neurosci *30*, 5334-5345.
Wilhite, B.L., Teyler, T.J., and Hendricks, C. (1986). Functional relations of the rodent claustral-entorhinal-hippocampal system. Brain Res *365*, 54-60.
Willems, J.G.P., Wadman, W.J., and Cappaert, N.L.M. (2018). Parvalbumin interneuron mediated feedforward inhibition controls signal output in the deep layers of the perirhinal-entorhinal cortex. Hippocampus *28*, 281-296.
Winter, J.D., Dorner, S., Lukovic, J., Fisher, J.A., St Lawrence, K.S., and Kassner, A. (2011). Noninvasive MRI measures of microstructural and cerebrovascular changes during normal swine brain development. Pediatr Res *69*, 418-424.
Winterer, J., Maier, N., Wozny, C., Beed, P., Breustedt, J., Evangelista, R., Peng, Y., D'Albis, T., Kempter, R., and Schmitz, D. (2017). Excitatory Microcircuits within Superficial Layers of the Medial Entorhinal Cortex. Cell Rep *19*, 1110-1116.
Witter, M.P., Doan, T.P., Jacobsen, B., Nilssen, E.S., and Ohara, S. (2017). Architecture of the Entorhinal Cortex A Review of Entorhinal Anatomy in Rodents with Some Comparative Notes. Front Syst Neurosci *11*, 46.
Witter, M.P., and Groenewegen, H.J. (1986). Connections of the parahippocampal cortex in the cat. IV. Subcortical efferents. J Comp Neurol *252*, 51-77.
Witter, M.P., Room, P., Groenewegen, H.J., and Lohman, A.H. (1986). Connections of the parahippocampal cortex in the cat. V. Intrinsic connections; comments on input/output connections with the hippocampus. J Comp Neurol *252*, 78-94.
Wouterlood, F.G., Hartig, W., Bruckner, G., and Witter, M.P. (1995). Parvalbumin-immunoreactive neurons in the entorhinal cortex of the rat: localization, morphology, connectivity and ultrastructure. J Neurocytol *24*, 135-153.
Woznicka, A., Malinowska, M., and Kosmal, A. (2006). Cytoarchitectonic organization of the entorhinal cortex of the canine brain. Brain Res Rev *52*, 346-367.
Wyss, J.M., Sripanidkulchai, B., and Hickey, T.L. (1983). An analysis of the time of origin of neurons in the entorhinal and subicular cortices of the cat. J Comp Neurol *221*, 341-357.

Ye, J., Witter, M.P., Moser, M.B., and Moser, E.I. (2018). Entorhinal fast-spiking speed cells project to the hippocampus. Proc Natl Acad Sci U S A *115*, E1627-E1636.
Yushkevich, P.A., Piven, J., Hazlett, H.C., Smith, R.G., Ho, S., Gee, J.C., and Gerig, G. (2006). User-guided 3D active contour segmentation of anatomical structures: significantly improved efficiency and reliability. Neuroimage *31*, 1116-1128.
Zhong, S., Zhang, S., Fan, X., Wu, Q., Yan, L., Dong, J., Zhang, H., Li, L., Sun, L., Pan, N., *et al.* (2018). A single-cell RNA-seq survey of the developmental landscape of the human prefrontal cortex. Nature *555*, 524-528.

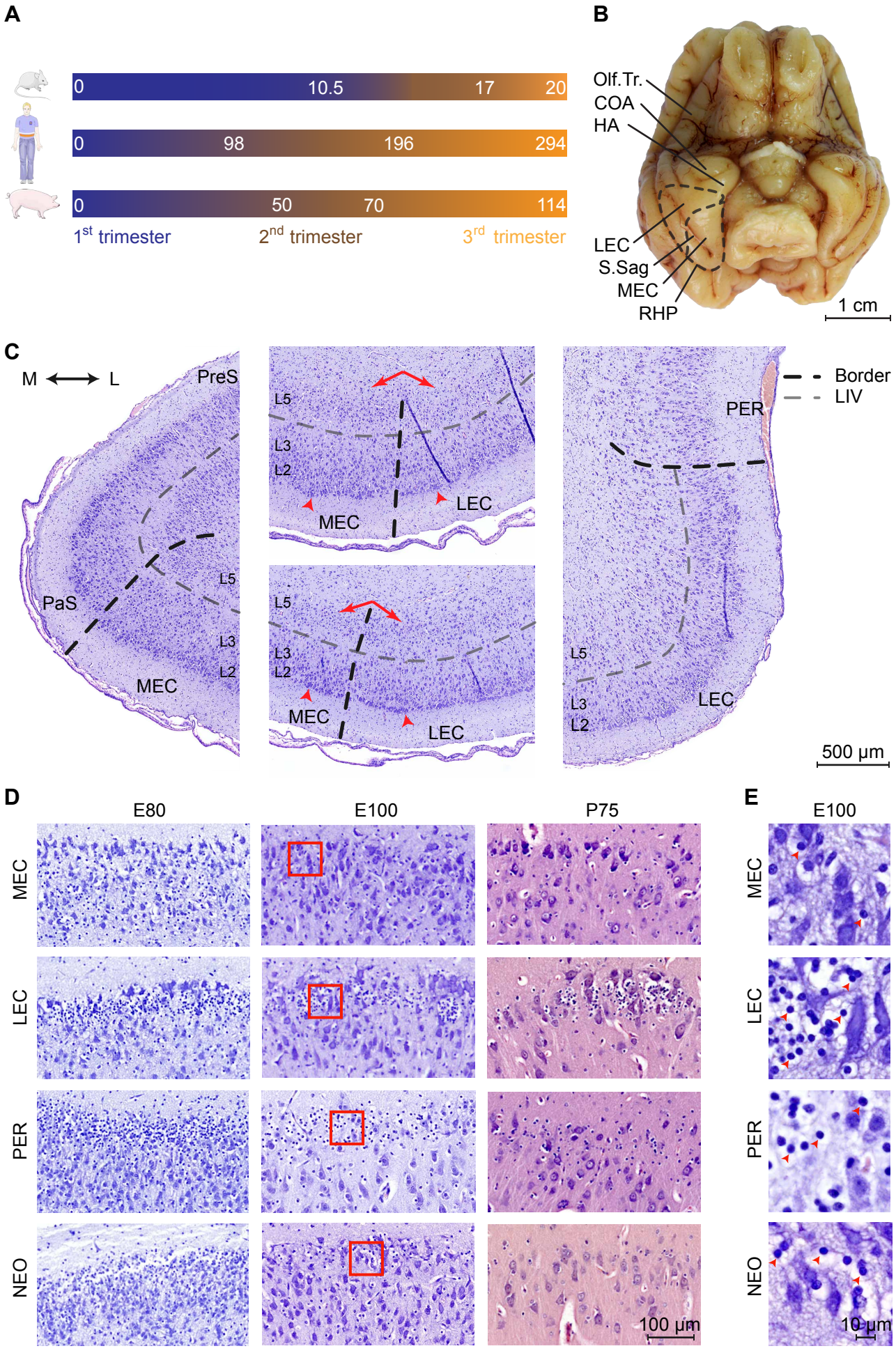
A
0
10.5
17
20
0
98
196
294
0
50
70
114
1st trimester
2nd trimester
3rd trimester
B
Olf.Tr.
COA
HA
LEC
S.Sag
MEC
RHP
1 cm
C
M
L
PreS
PaS
MEC
L5
L3
L2
LEC
PER
Border
LIV
500 µm
D
E80
E100
P75
MEC
LEC
PER
NEO
100 µm
E
E100
10 µm

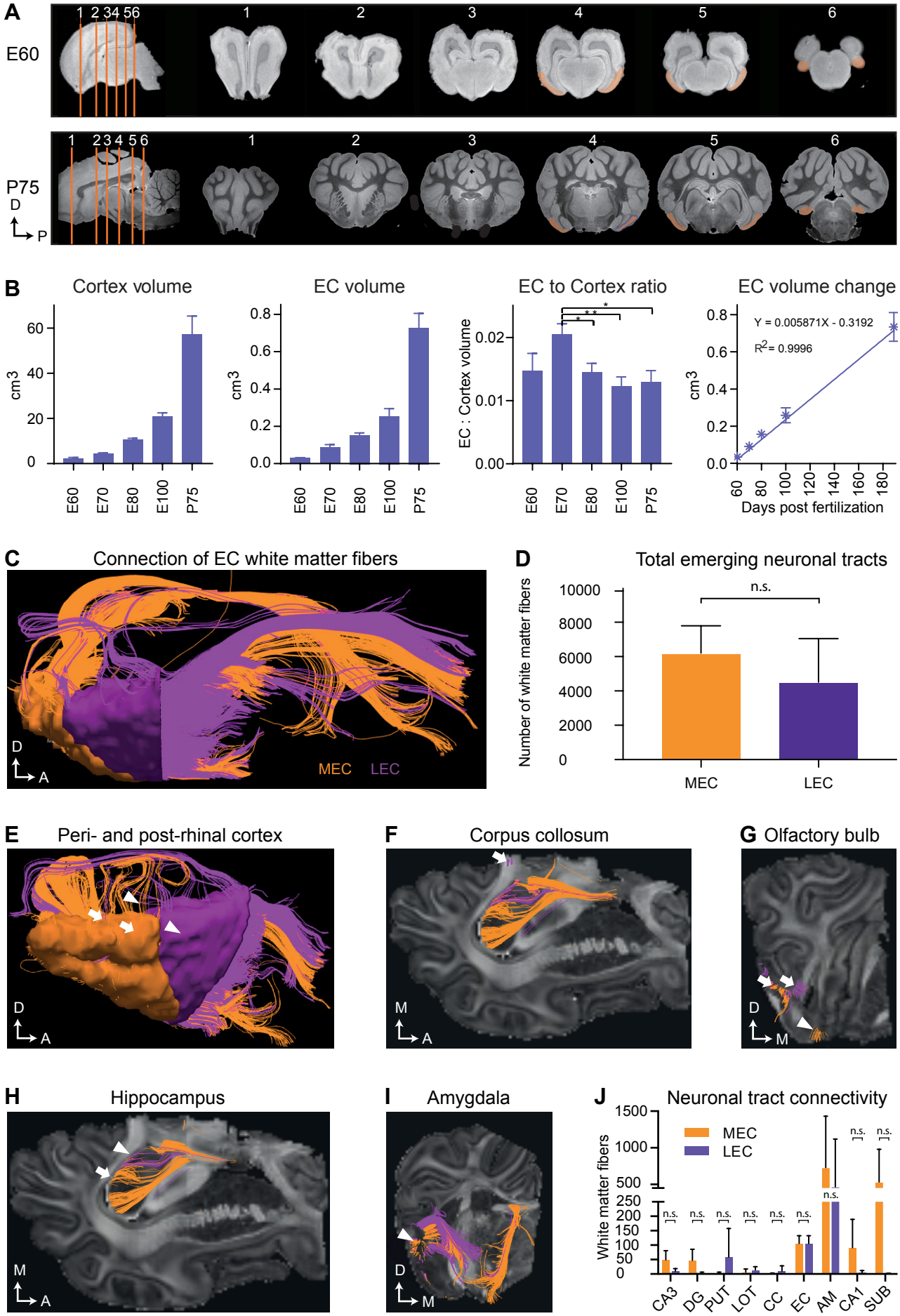
A
E60
P75
D
P
B
Cortex volume
EC volume
EC to Cortex ratio
EC volume change
cm3
EC : Cortex volume
Y = 0.005871X - 0.3192
R2= 0.9996
Days post fertilization
E60
E70
E80
E100
P75
C
Connection of EC white matter fibers
MEC
LEC
D
Total emerging neuronal tracts
Number of white matter fibers
n.s.
MEC
LEC
E
Peri- and post-rhinal cortex
F
Corpus collosum
G
Olfactory bulb
H
Hippocampus
I
Amygdala
J
Neuronal tract connectivity
White matter fibers
MEC
LEC
CA3
DG
PUT
LOT
CC
EC
AM
CA1
SUB

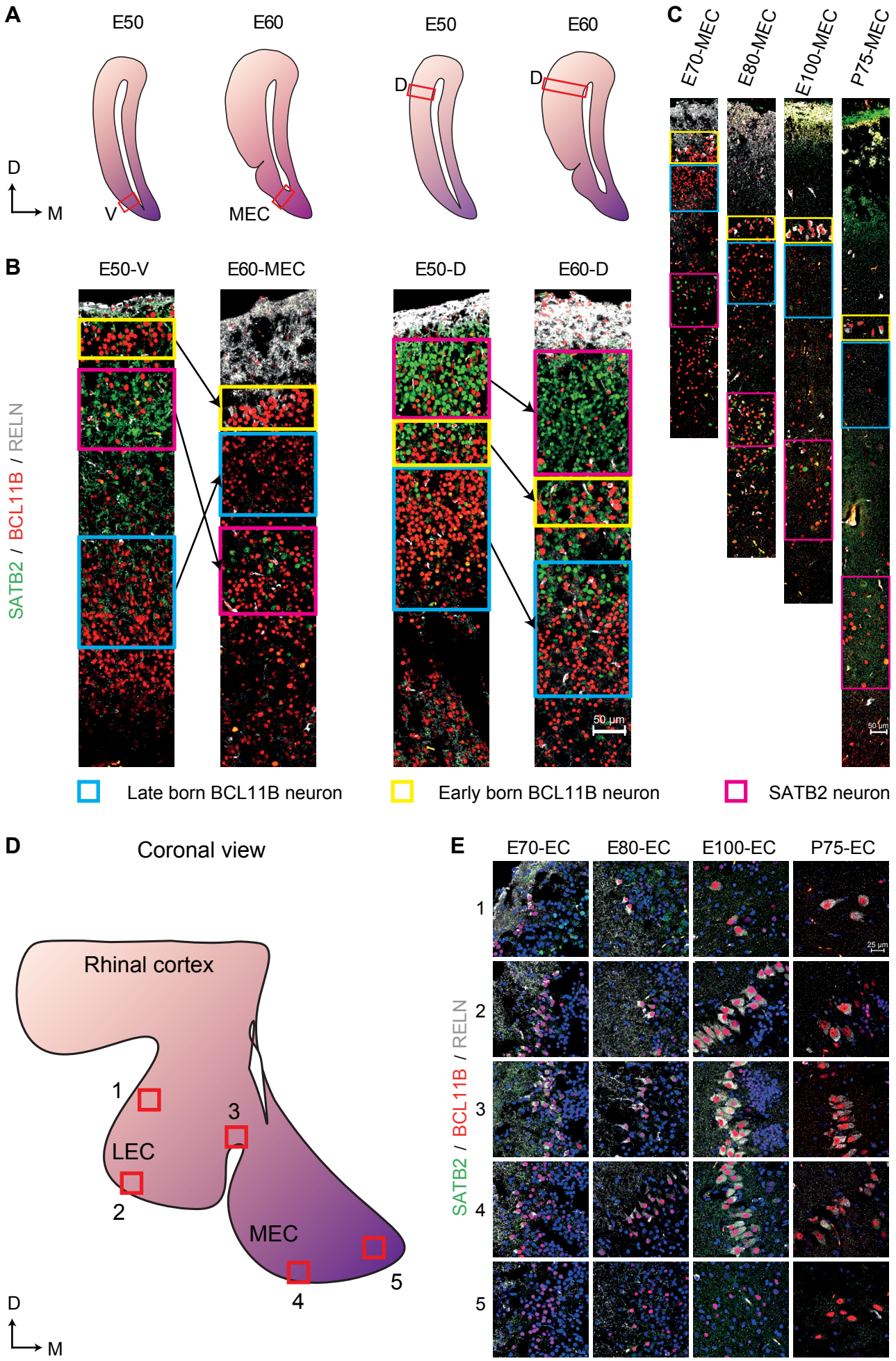
A
E50
E60
E50
E60
D
M
V
MEC
D
D
B
E50-V
E60-MEC
E50-D
E60-D
SATB2 / BCL11B / RELN
50 µm
C
E70-MEC
E80-MEC
E100-MEC
P75-MEC
50 µm
Late born BCL11B neuron
Early born BCL11B neuron
SATB2 neuron
D
Coronal view
Rhinal cortex
1
2
3
4
5
LEC
MEC
D
M
E
E70-EC
E80-EC
E100-EC
P75-EC
1
2
3
4
5
SATB2 / BCL11B / RELN
25 µm

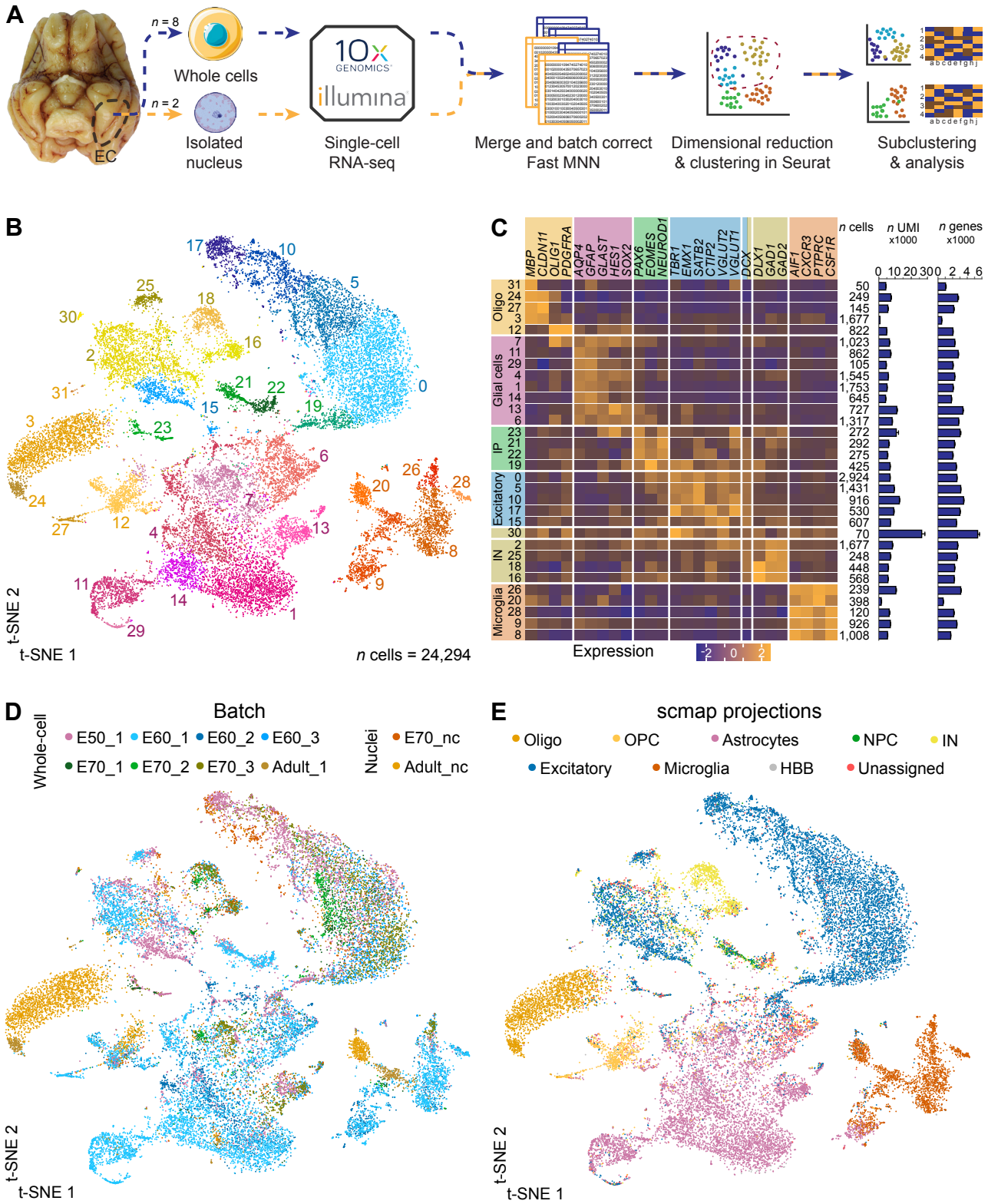
A
n = 8
Whole cells
n = 2
Isolated nucleus
EC
10x GENOMICS
illumina
Single-cell RNA-seq
Merge and batch correct Fast MNN
Dimensional reduction & clustering in Seurat
Subclustering & analysis
B
t-SNE 1
t-SNE 2
n cells = 24,294
C
MBP CLDN11 OLIG1 PDGFRA AQP4 GFAP GLAST HES1 SOX2 PAX6 EOMES NEUROD1 TBR1 EMX1 SATB2 CTIP2 VGLUT2 VGLUT1 DCX DLX1 GAD1 GAD2 AIF1 CXCR3 PTPRC CSF1R
n cells
n UMI x1000
n genes x1000
Oligo
Glial cells
IP
Excitatory
IN
Microglia
Expression
D
Batch
Whole-cell
E50_1 E60_1 E60_2 E60_3
E70_1 E70_2 E70_3 Adult_1
Nuclei
E70_nc
Adult_nc
t-SNE 1
t-SNE 2
E
scmap projections
Oligo OPC Astrocytes NPC IN
Excitatory Microglia HBB Unassigned
t-SNE 1
t-SNE 2

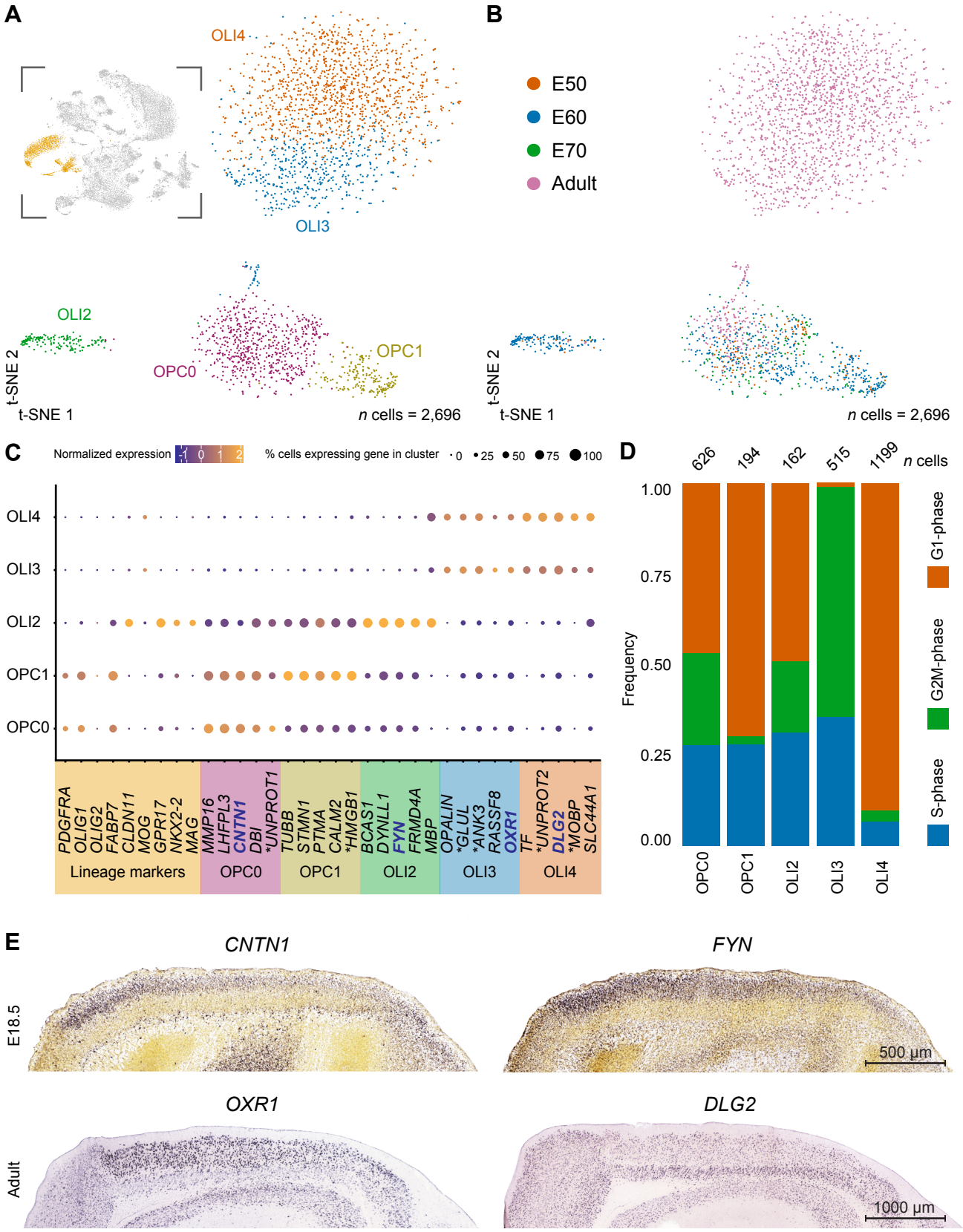
A
OLI4
OLI3
OLI2
OPC0
OPC1
t-SNE 2
t-SNE 1
n cells = 2,696
B
E50
E60
E70
Adult
t-SNE 2
t-SNE 1
n cells = 2,696
C
Normalized expression
% cells expressing gene in cluster
0
25
50
75
100
OLI4
OLI3
OLI2
OPC1
OPC0
PDGFRA
OLIG1
OLIG2
FABP7
CLDN11
MOG
GPR17
NKX2-2
MAG
MMP16
LHFPL3
CNTN1
DBI
*UNPROT1
TUBB
STMN1
PTMA
CALM2
*HMGB1
BCAS1
DYNLL1
FYN
FRMD4A
MBP
OPALIN
*GLUL
*ANK3
RASSF8
OXR1
TF
*UNPROT2
DLG2
*MOBP
SLC44A1
Lineage markers
OPC0
OPC1
OLI2
OLI3
OLI4
D
626
194
162
515
1199
n cells
Frequency
1.00
0.75
0.50
0.25
0.00
G1-phase
G2M-phase
S-phase
OPC0
OPC1
OLI2
OLI3
OLI4
E
CNTN1
FYN
E18.5
500 µm
OXR1
DLG2
Adult
1000 µm

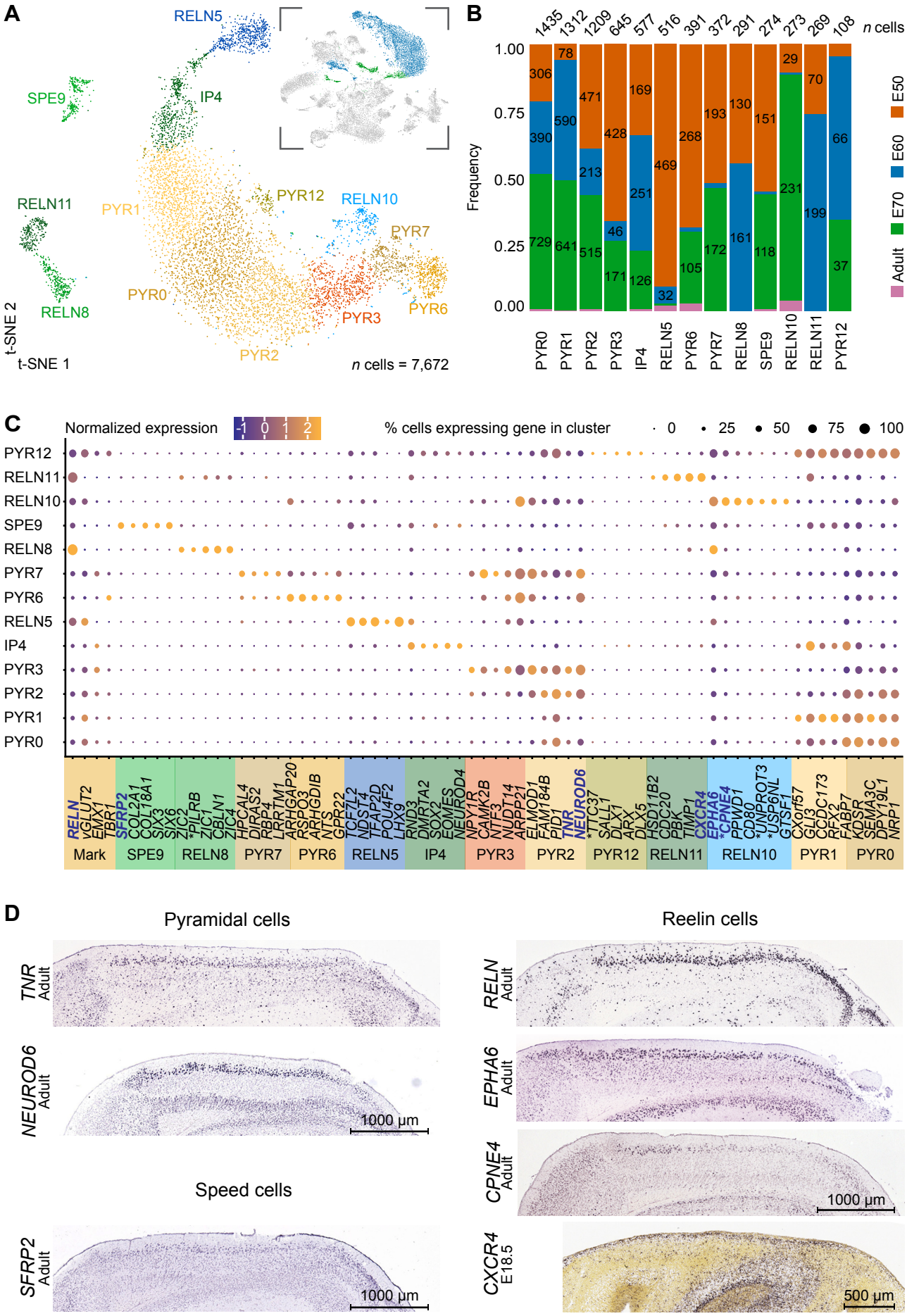
A
RELN5
SPE9
IP4
RELN11
PYR1
PYR12
RELN10
PYR7
PYR0
RELN8
PYR3
PYR6
PYR2
t-SNE 2
t-SNE 1
n cells = 7,672
B
1435 1312 1209 645 577 516 391 372 291 274 273 269 108 n cells
Frequency
1.00
0.75
0.50
0.25
0.00
E50
E60
E70
Adult
PYR0 PYR1 PYR2 PYR3 IP4 RELN5 PYR6 PYR7 RELN8 SPE9 RELN10 RELN11 PYR12
C
Normalized expression
-1 0 1 2
% cells expressing gene in cluster
0 25 50 75 100
PYR12
RELN11
RELN10
SPE9
RELN8
PYR7
PYR6
RELN5
IP4
PYR3
PYR2
PYR1
PYR0
RELN VGLUT2 EMX1 TBR1
SFRP2 COL2A1 COL18A1 SIX3 SIX6
ZIC2 *PILRB ZIC1 CBLN1 ZIC4
HPCAL4 DIRAS2 RBP4 LRRTM1 ARHGAP20 RSPO3 ARHGDIB NTS GPR22
TCF7L2 NDST4 TFAP2D POU4F2 LHX9
RND3 DMRTA2 SOX2 EOMES NEUROD4
NPY1R CAMK2B NTF3 NUDT14 ARPP21
ELMOD1 FAM184B PID1 TNR NEUROD6
*TTC37 SALL1 DLX1 ARX DLX5
HSD11B2 CDC20 PBX TIMP1 CXCR4
EPHA6 *CPNE4 PPWD1 CD80 *UNPROT3 *USP6NL GTSE1
CXorf57 GLI3 CCDC173 RFX2 FABP7
KDSR SEMA3C DPY19L1 NRP1
Mark SPE9 RELN8 PYR7 PYR6 RELN5 IP4 PYR3 PYR2 PYR12 RELN11 RELN10 PYR1 PYR0
D
Pyramidal cells
TNR Adult
NEUROD6 Adult
1000 µm
Speed cells
SFRP2 Adult
1000 µm
Reelin cells
RELN Adult
EPHA6 Adult
CPNE4 Adult
1000 µm
CXCR4 E18.5
500 µm

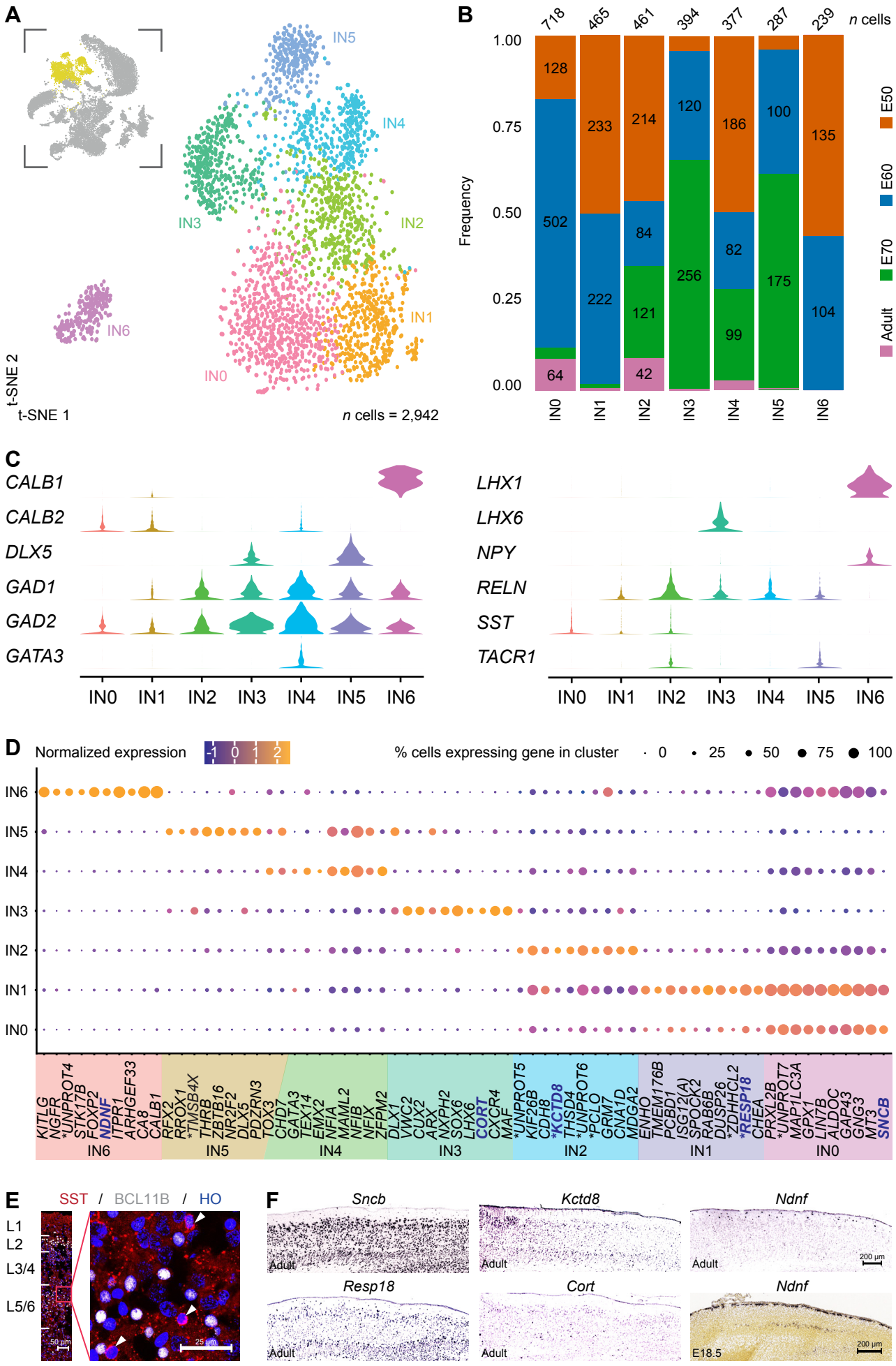
A
IN5
IN4
IN3
IN2
IN1
IN6
IN0
t-SNE 2
t-SNE 1
n cells = 2,942
B
718
465
461
394
377
287
239
n cells
Frequency
1.00
0.75
0.50
0.25
0.00
128
502
64
233
222
214
84
121
42
120
256
186
82
99
100
175
135
104
E50
E60
E70
Adult
IN0
IN1
IN2
IN3
IN4
IN5
IN6
C
CALB1
CALB2
DLX5
GAD1
GAD2
GATA3
LHX1
LHX6
NPY
RELN
SST
TACR1
IN0
IN1
IN2
IN3
IN4
IN5
IN6
D
Normalized expression
-1
0
1
2
% cells expressing gene in cluster
0
25
50
75
100
IN6
IN5
IN4
IN3
IN2
IN1
IN0
KITLG
NGFR
*UNPROT4
STK17B
FOXP2
NDNF
ITPR1
ARHGEF33
CA8
CALB1
RFX2
RROX1
*TMSB4X
THRB
ZBTB16
NR2F2
DLX5
PDZRN3
TOX3
CHD7
GATA3
TEX14
EMX2
NFIA
MAML2
NFIB
NFIX
ZFPM2
DLX1
VWC2
CUX2
ARX
NXPH2
SOX6
LHX6
CORT
CXCR4
MAF
*UNPROT5
KIF26B
CDH8
*KCTD8
THSD4
*UNPROT6
*PCLO
GRM7
CNA1D
MDGA2
ENHO
TMEM176B
PCBD1
ISG12(A)
SPOCK2
RAB6B
DUSP26
*ZDHHC2
*RESP18
CHEA
PRXL2B
*UNPROT7
MAP1LC3A
GPX1
LIN7B
ALDOC
GAP43
GNG3
MT3
SNCB
E
SST / BCL11B / HO
L1
L2
L3/4
L5/6
50 µm
25 µm
F
Sncb
Kctd8
Ndnf
Resp18
Cort
Ndnf
Adult
E18.5
200 µm